Lacunar-Canalicular Bone Remodeling and Its Impact on Bone Quality: Imaging and Diagnostic Assessment Tools in Skeletal Health

Dr. Sofia Almeida[1]*

[1]Hospital Clínico San Carlos, Department of Orthopedic Research, Madrid, Spain

Abstract

Osteocytes can resorb as well as replace bone adjacent to the expansive lacunar-canalicular system (LCS). Suppressed LCS remodeling decreases bone fracture toughness, but it is unclear how altered LCS remodeling impacts bone quality. The first goal of this review is to assess how LCS remodeling impacts LCS morphology as well as the composition and mechanical properties of surrounding bone tissue. The second goal is to compare tools available for the assessment of bone quality at length-scales that are physiologically-relevant to LCS remodeling. We find that changes to LCS morphology occur in response to a variety of physiological conditions and diseases and can be classified in two general phenotypes. In the ‘aging phenotype’, seen in aging and in some disuse models, the LCS is truncated and osteocytes apoptosis is increased. In the ‘osteocytic osteolysis’ phenotype, which is adaptive in some physiological settings and possibly maladaptive in others, the LCS enlarges and osteocytes generally maintain viability. Bone composition and mechanical properties vary near the osteocyte and change with at least some conditions that alter LCS morphology. However, few studies have evaluated bone composition and mechanical properties close to the LCS and so the impacts of LCS remodeling phenotypes on bone tissue quality are still undetermined. We summarize the current understanding of how LCS remodeling impacts LCS morphology, tissue-scale bone composition and mechanical properties, and whole-bone material properties. Tools are compared for assessing tissue-scale bone properties, as well as the resolution, advantages, and limitations of these techniques.

Keywords

Osteocyte; lacunar-canalicular system; bone remodeling; bone mineralization; bone quality

Introduction

Osteocytes are terminally-differentiated osteoblasts that reside in holes in the bone matrix termed lacunae. Dendritic processes from the cell wall extend through a network of canaliculi to form gap junctions with other osteocytes.[1–3] The osteocyte performs many functions, including mechanotransduction, coordination of osteoclasts and osteoblasts, and participation in systemic mineral homeostasis.[1–3] In recent years, the lacunar-canalicular system (LCS) is acknowledged to directly participate in bone tissue remodeling. The impact of LCS remodeling on bone tissue composition and mechanical properties is potentially very significant. There are ~42 billion osteocytes in the adult human (>20 years old) skeleton[4], with 20-126 canaliculi each[4–8], which together have a surface area of ~215 m^2.[4] The expansive network of bone that can potentially undergo LCS remodeling far exceeds the surface available for remodeling by osteoclasts and osteoblasts.[9]

The first observations that the osteocyte can modify surrounding bone matrix were made more than 50 years ago by Belanger, who reported proteolytic activity in mature osteocytes.[10] The first of many reports of altered LCS remodeling were for osteocytic osteolysis – the enlargement of lacunae and canaliculi.[10–14] In the last decade, interest in LCS remodeling has greatly increased. It is now identified that altered LCS remodeling can also contract, as opposed to expand, lacunar and canalicular morphologies.[15–19] Several mechanisms are now identified for how osteocytes modify their surrounding bone tissue environment. Osteocytes resorb bone by acidification[20], as well as by production of matrix metalloproteinases[12,21–23], cathepsin K[12,24], and tartrate-resistant acid phosphatase.[12,25] Osteocytes can build bone by deposition of new osteoid.[12,25,26] Bone resorption and deposition occurs along the osteocyte lacuna as well as along dendrites extending into canaliculi.[12,27,28]

LCS remodeling has the potential to impact bone tissue maturity, the effective age of a packet of bone tissue.[29] With time from osteoid deposition, bone tissue undergoes rapid primary mineralization (days) and then slower secondary mineralization (months).[29,30] Mineral characteristics also change with maturity; more mature hydroxyapatite crystals are larger, more perfect, and have increased carbonate substitution.[31,32] Enzymatic and non-enzymatic collagen crosslinks both accumulate in the maturating tissue.[33] More mature tissue is compositionally less heterogeneous[34,35] and has increased microcracks.[36] Conventionally, bone tissue maturity is considered to result from a balance between osteoblastic deposition and osteoclastic resorption.[29] Because the osteocyte can both resorb and replace bone, it is possible that tissue maturity can be ‘refreshed’ for tissue adjacent to lacunar and canaliculi by more frequent LCS remodeling.

A growing body of knowledge demonstrates that LCS morphologies change in aging, unloading, estrogen deficiency and other conditions that lower bone fracture resistance.[15–19,37–39] Several questions need to be addressed to improve the understanding of the role of the LCS in tissue-scale bone quality and

whole-bone fracture resistance. First – what is the impact of altered LCS remodeling on tissue-scale bone tissue composition and mechanical properties? Second – when are changes to LCS remodeling adaptive versus maladaptive from the perspective of bone quality maintenance? These questions currently complicate interpreting the significance of altered LCS morphologies that occur in many physiological conditions.

The purpose of this Review is to summarize current knowledge about the role of the LCS and its regulation of bone tissue quality. We consider the current state of knowledge about how LCS remodeling affects network morphology, bone tissue composition and mechanical properties, and the impacts of these tissue-scale changes to whole-bone material properties. In addition, we compare the advantages, limitations, and resolution of tools available to study bone quality local to the LCS. Finally, we address current gaps of knowledge to drive future directions.

1. The significance of LCS remodeling on bone quality and fracture resistance.

1.1 Does LCS remodeling and perilacunar bone quality impact bone fracture resistance?

Genetic mouse models suggest that reduced LCS remodeling, which is sometimes termed perilacunar remodeling (PLR) or perilacunar-canalicular remodeling (PLCR) diminishes bone quality and fracture toughness.[23,40,41] Mouse models producing a phenotype of decreased LCS remodeling concurrent with decreased notched fracture toughness include MMP13$^{-/-}$ [40] and DMP1-Cre$^{+/-}$; TGFβ$^{fl/fl}$ [23], both in 2-month old male mice. DMP1-Cre$^{+/-}$;MMP13$^{fl/fl}$ does not reduce bone work to failure from three-point bending in 2-month or 4-month male mice[42], although this quantification of bone toughness is known to be more variable that notched fracture toughness.[43] Together, these genetic models implicate the TGFβ pathway in the maintenance of bone fracture resistance. The specific reasons why diminished LCS remodeling affects fracture resistance in these models are not clear. These models result in reduced perilacunar bone resorption or deposition[40,42] and also result in smaller lacunar morphology[23,42], increased nonenzymatic collagen crosslinks[40], and decreased flexural and tissue-scale moduli[23], all of which have the potential to impact whole-bone fracture resistance. These models are a compelling basis for considering that LCS remodeling is important for bone quality, but there several important gaps in understanding. First, the relationship between LCS bone remodeling and fracture resistance is not clear. For example, it is not reported if conditional knock out mice have a positive correlation between LCS remodeling and fracture resistance, and if this relationship would also be detected in wild type mice. Second, these deletions occur while the skeleton is growing, which may confound the role of the osteocyte in development versus maturity in maintaining bone tissue quality. Ultimately, it is not yet understood if LCS remodeling is important for maintaining bone quality and fracture resistance in health, as well as what would constitute a deleterious alteration to the frequency or extent of this remodeling. As

reviewed in subsequent sections, LCS network geometries as well as the composition and mechanical properties of bone tissue local to the LCS may all change in response to altered remodeling (**Table 1**). These changes, in turn, may influence whole-bone mechanics, including fracture resistance.

1.2 The impact of LCS remodeling on LCS morphology

The role of the osteocyte in remodeling bone tissue is currently most studied from the perspective of LCS morphology, which is readily assessed using a number of imaging techniques. Osteocytes participate in calcium homeostasis, partly through PTHrP stimulation, by resorbing bone surrounding lacunae and canaliculi to liberate calcium.[20] Osteocyte lacunae and canaliculi enlarge for lactating C57Bl/6 and CD1 mice, and then recover after weaning, indicating that osteocytes are capable of producing bone matrix.[12,28,38] However, the effects of lactation on lacunae may depend on the genetic strain of the animals tested. For example, Naval Medical Research Institute (NMRI) mice[44] do not undergo lacunar morphological changes with lactation. Some of these effects could also relate to litter size, as smaller litter sizes (which occur with some strains) produce less calcium demand for the lactating mother.[45–47] Exogenous parathyroid hormone (PTH) treatment stimulates calcium release and affects lacunar geometries. Lacunae enlarge for Wistar rats treated continuously[14] or C57Bl/6 mice treated intermittently[48] with PTH (1,34). Intermittently elevated PTH due to exercise may only have a mild effect on lacunar morphology in areas that are receiving sufficient baseline mechanical loading, but this requires further investigation.[49] Lacunar morphologies are also responsive to disruptions in phosphate homeostasis. The underlying pathologic conditions in these studies complicates interpretations of the involvement of LCS remodeling. For example, osteocyte lacunae are larger for mice with x-linked hypophosphatemia than for wild type controls.[50] LCS remodeling could be altered, but these results could also be related to global differences in phosphate availability and bone mineralization. Lacunar morphology appears to be altered in chronic kidney disease (CKD), which affects phosphate homeostasis. In humans, iliac crest biopsies from patients with high-turnover CKD do not have different lacunar areas from low-turnover CKD, but do have increased lacunar number density, perimeter, and porosity. Further, lacunar number density and area were positively correlated with serum PTH.[51] However, it is important to note that it is not yet clear whether changing lacunar morphologies in CKD are a product of altered phosphate levels or may instead reflect changes from other features of the disease, including inflammation and oxidative stress.

Lacunar morphologies also change with aging and this appears to be conserved across species. 3D measurements reveal that aged mice (24 mo) have less-abundant osteocyte lacunae compared with skeletally-mature young mice (6 mo), and are smaller, rounder, and less-oriented (**Figure 2**).[15,52] Lacunar number density declines with aging for male[15,16] and female[16] mice, which recapitulates the same effect in

humans.[53–56] Further, an association between increased age and decreased lacunar volume and increased lacunar roundness is seen for mice at several load-bearing skeletal sites[15,16,37] as well as for female humans.[57] These effects are dependent on sex; female 22 month-old mice have smaller osteocyte cell volume but not lacunar volume compared with 5 month-old comparisons, yet males have decreased lacunar volume over the same time period.[16] The canalicular network also degenerates with aging. Canalicular and dendrite numbers each decrease with aging in male and female mice.[16] It is unclear why aging produces changes to LCS morphology, but the increased osteocyte apoptosis, autophagy, and senescence in aging may have roles in these network changes due to the accompanying loss of mechanical sensitivity.[58–60]

Lacunar morphologies appear to be sensitive to unloading. Common models of disuse and the osteocyte include sciatic neurectomy, hindlimb unloading, Botox immobilization, and microgravity.[17–19,61,62] These studies mostly agree that unloading results in smaller and more spherical lacunae and increased osteocyte apoptosis. In a study of 30-week female Sprague Dawley rats, sciatic neurectomy at 3 weeks of age reduced both lacunar volume and number density.[18] Hindlimb unloading of 6 mo old male Sprague Dawley rats for 28 days increased osteocyte apoptosis and decreased lacunar number density.[19] Additionally, 1 month of spaceflight for 23-week old C57Bl/6N male mice also resulted in smaller, more spherical, and less-abundant lacunae, as well as increased fraction of empty lacunae.[17] However, not all unloading studies find this ‘aging’ phenotype. In a study of 14-week old Wistar female rats administered Botox in a hindlimb, osteocyte lacunar size, shape, and density were not affected in a 28-week period following injection.[61] Spaceflight can also produce an osteocytic osteolysis phenotype. Female C57Bl6/mice subjected to 15 days of flight had larger and more elongated lacunae in ischial cortical bone, with no evidence of osteocyte death.[62]

Exercise does not have a simple relationship with LCS morphology. Aerobic exercise causes an increase in PTH to counteract the loss of ionized calcium, which occurs in the first couple of minutes of exercise and persists until the end of the bout of exercise.[63,64] However, aerobic exercise does not clearly increase lacunar size.[49] Lacunar area was not significantly increased for 16-week old C57Bl/6 mice subjected to 30-min of running for 21 days, although the perilacunar bone was significantly less mineralized[49] (reviewed in section 1.4). Zebrafish exercised in a swim tunnel for 4 weeks had similar lacunar volume and sphericity in vertebral bone compared with non-exercised controls.[65] Importantly, the effect of exercise paradigms that engender high mechanical strains (e.g., resistance training, jumping) on LCS has not been tested. Resistance training decreases PTH during the exercise and jumping decreases PTH after exercise, which may further affect the osteocyte in comparison with aerobic training.[66,67] Ultimately, the paucity of studies about the effects of loading and unloading on LCS remodeling, as well

as inconsistent loading/unloading models, species, skeletal site, sex and age of study animals across investigations contribute to a persistant gap in understanding about the effects of loading on the osteocyte.

Both estrogen deficiency[68] and antiresorptives[69] affect osteocyte viability and behavior, and so several investigations assessed whether OVX or common osteoporosis treatments also affect osteocyte lacunar morphologies. Lane and coworkers found that osteocyte lacunae were ~5% larger at 21 days after OVX for 6 month old Swiss-Webster mice compared with sham controls.[39] Sharma *et al* found increased lacunar-canalicular porosity and canalicular diameter, but no change in lacunar number density for Sprague Dawley rats 6 weeks from OVX versus sham controls.[70] However, OVX is not always found to influence the LCS. Stern and coworkers found that lacunar sizes and number density were not different 8 weeks after OVX, with or without sequential osteoporosis treatment, for 6 month Sprague Dawley rats compared with sham controls.[71]

Data across physiological models suggest that the osteocyte could have 'adaptive' and 'maladaptive' responses to changing physiological conditions (**Figure 1**). The 'aging' phenotype of smaller and more spherical lacunae, together with increased apoptosis, is likely maladaptive. This phenotype appears in aging[15,16] and unloading[18,19] and sometimes appears in spaceflight[17] and glucocorticoid therapy.[21] It is not clear whether this phenotype emerges because of increased senescence, apoptosis, inflammation, osteocyte metabolic dysfunction, of some combination of these events. It is further unclear whether the 'aging' phenotype is caused by, or instead causes, impaired mechanosensation. A separate phenotype of abundant large and elongated lacunae is not clearly adaptive nor maladaptive. Sometimes, this 'osteocytic osteolysis' phenotype may be adaptive, as for lactation[12,28] or PTH treatment.[48] Other times, this phenotype may be maladaptive. For instance, in high-turnover CKD, lacunar size is positively correlated with serum PTH[51], and LCS remodeling increases.[26] Interestingly, this phenotype is generally not associated with apoptosis, indicating a continued active role of the osteocyte whether in health or disease. There may be additional adaptive functions of the 'osteocytic osteolysis' phenotype. From FEA results (reviewed in 1.7), increased lacunar size and decreased perilacunar tissue modulus, which often accompanies increased lacunar size, both increase perilacunar tissue strain.[71,72] It is possible that osteocytes may be able to amplify local bone tissue strains, which could sometimes represent an adaptive functionality. Studies that investigate LCS geometries together with perilacunar bone composition are needed for better contextualizing whether LCS remodeling is adaptive or maladaptive in particular physiological conditions. Further, the region of bone investigation should be carefully decided. Lamellar bone has fewer but larger and more elongated lacunae, while woven bone has more lacunae which are also more spherical and randomly oriented.[73] Thus, lacunar morphological differences in diseases that increase woven bone formation, such as diabetes and obesity, may be a reflection of the

differences in bone tissue organization as opposed to an indication of adaptive or maladaptive osteocyte response.[74,75]

1.3 The LCS and bone mineralization

The distribution of hydroxyapatite mineral in bone tissue is not homogenous and is impacted by proximity to the LCS. Most bone mineral is located within 1.2-1.4 micrometers of a canalicula.[76,77] Bone mineral quantity appears to be graded within the immediate vicinity of the LCS.[27,76–78] Hesse *et al* studied human jaw bone specimens from adult donors (ages 19-72) that were healthy or had bisphosphonate-induced osteonecrosis with synchrotron x-ray computed tomography.[76] Most mineral was located very close (< 0.5 μm) to canaliculi and lacunae, and then mineral density decreased radially outwards until reaching asymptotic values. Mineral gradients were more profound for healthy patients than for those with osteonecrosis, in which case there was less contrast between the high mineralization alongside the LCS walls and the mineral-saturated osteonecrotic bone matrix. These data suggest that a larger mineral gradient is indicative of recent or continuous remodeling. Another study, by Kerschnitzki and coworkers, assessed healthy ovine cortical bone with both CLSM and synchrotron small-angle x-ray scattering and determined that hydroxyapatite mineral platelets were thicker alongside the LCS.[77] Minerals were larger and more oriented in regions with denser lacunae and canaliculi. Also in support of higher mineral adjacent to lacunae, Gardinier *et al* found that the first 2.5 μm-thick concentric ring away from the lacunar wall in male control C57Bl/6 mice had higher backscattered scanning electron microscopy (BSEM) grey level and thus mineralization when compared with bone further from the lacuna.[49]

Not all studies agree that mineral density is greatest at the LCS boundary. Nango and coworkers, using synchrotron x-ray CT and also transmission electron microscopy (TEM), found the opposite effect in terms of mineral graduation and distance from canaliculi.[27] These authors studied healthy adult C57Bl/6 mice, as well as mice that were lactating, receiving PTH treatment, or osteopetrotic. In all conditions studied, mineral density was lowest in the hundreds of nanometers alongside the canalicular wall and gradually increased within the first 2 micrometers. Similar mineralization gradients were found around lacunae, including some with higher mineralization local to the lacuna wall. In agreement with these findings, Kaya *et al* reported that bone mineralization assessed by backscattered electron microscopy was decreased near canaliculi for both lactating and control mice.[28] Importantly, the tissue age for lacunae and canaliculi with these different mineralization profiles is not determined. It is possible that high- or low-mineralization adjacent to the LCS is an indicator of tissue maturation (i.e., lower mineralization indicates recent remodeling) but this idea requires investigation.

Comparisons of mineralization between bone adjacent and farther away from the LCS are probably dependent on the choice of technique. For example, while BSEM, synchrotron x-ray CT, and TEM find mineral gradients near the LCS in healthy bone[27,28,49,76,77], Raman spectroscopy studies often do

not find differences in mineralization between perilacunar and non-perilacunar bone except for extreme osteocyte osteolysis phenotypes.[39,48,49,79] Part of this discrepancy might be that most Raman spectroscopy studies have termed the first 5 μm line of bone extending from the lacunar wall the 'perilacunar' region[48,49,79], while high-resolution imaging demonstrates that most of the mineral gradient exists within the first micrometer from the LCS.[27,76,77] Indeed, Gardinier *et al* found no difference in mineral:matrix or carbonate:phosphate between perilacunar and non-perilacunar bone in sedentary controls (not treated with PTH) rats for the same study that found higher mineral in the first 2.5 μm near lacunae using BSEM.[49]

The LCS may also participate in the process of bone tissue mineralization. Finite element modeling of bone primary and secondary mineralization demonstrates that diffusion alone cannot account for the amount of calcium transported from a Haversian canal surface to mineralizing bone tissue.[30] Some experimental data supports the concept of the LCS participating in bone mineralization. In a study of rhodamine-stained femur sections from female adults and children, mineral density measured from quantitative backscattered electron imaging (qBEI) was increased in osteons with greater canalicular network length.[80] However, whether the LCS has passive or active roles in bone mineralization is yet to be determined.

1.4 The impact of altered LCS remodeling on bone composition

Altered LCS remodeling may affect either bone mineral content, mineral maturity, or both. Not surprisingly, conditions associated with calcium homeostasis and the 'osteocytic osteolysis' lacunar phenotype can produce lower mineralization near the LCS.[27,28,39] When glucocorticoid treatment produces this phenotype, profound hypomineralization halos are detected in 25 μm-radius regions surrounding lacunae.[39] PTH(1,34) treatment of young adult male C57Bl/6J mice increases lacunar area and decreases bone mineralization in the first 5 μm of perilacunar bone compared with bone farther away.[48] Exercise does not significantly increase lacunar size, but does decrease mineral:matrix from Raman spectroscopy in the first 5 μm of perilacunar bone compared with sedentary mice.[49] Interestingly, while the expansion of lacunae and canaliculi during lactation inherently imply mineral resorption, changes to peri-LCS bone tissue mineralization in lactation are not greater than for non-lactating controls.[27,28] Thus, osteocytic osteolysis is not necessarily associated with detectable differences in bone mineralization near the LCS.

In some cases, altered mineral maturity is observed for the 'osteocytic osteolysis' phenotype. Differences were not detected in Raman spectroscopy mineral:matrix or BSEM mineralization for lactating, 1-week post weaning, and control C57Bl/6 mice, but a decrease in carbonate:phosphate was detected for lactating mice when compared with controls.[28] These measurements were not collected for bone immediately adjacent to the LCS but were instead collected away from periosteal and endocortical forming surfaces, suggested that this change in bone composition were nonetheless the result of altered

LCS remodeling. After 21 days of exercise for male C57Bl/6 mice, perilacunar bone (first 5 μm from lacunar wall) had lower mineral:matrix and higher carbonate:phosphate than sedentary controls.[49] PTH(1,34) treatment, meanwhile, decreased carbonate:phosphate in male C57Bl/6 mice.[48] Changes in mineral maturity may have a different meaning for LCS remodeling than changes in mineralization. Decreased carbonate:phosphate indicates lower average mineral maturity, and thus this may indicate that bone replacement is relatively frequent.[32,81] Alternatively, lower carbonate:phosphate may indicate recent bone resorption, as hydroxyapatite with higher carbonate substitution may dissolve first.[28,81]

To our knowledge, bone tissue composition has not been studied around lacunae or canaliculi in aging or in disease models that produce the 'aging' phenotype of LCS remodeling. However, infilling of osteocyte lacunae with dense mineral is noted to occur in studies of aged human bone.[53] The lack of compositional data corresponding to this phenotype of altered LCS remodeling represents a major gap in knowledge that may yield insights into maintenance of skeletal fracture resistance through the lifespan.

1.5 *The impact of LCS remodeling on bone tissue mechanical properties*

Bone mechanical properties vary surrounding the LCS (**Figure 3**). Zhang and colleagues[82] used nanoindentation and atomic force microscopy (AFM) to map moduli for lacunae and canaliculi for 4-month old female Wistar rats. Moduli were lower and more variable for 1-5 μm thick non-concentric regions adjacent to lacunae. The modulus of peri-canalicular bone was also lower adjacent to canaliculi, although the modulus increased with distance down the canaliculi, away from the lacunar wall. For some studies, modulus appears to vary more than bone tissue composition with distance from the LCS.. Stern and coworkers[71] studied sham or OVX rats treated with various sequences of osteoporosis drugs or vehicle. Six-linear profiles extending 20 μm (1 μm spacing) were placed for each studied lacuna. For sham rats, the modulus of bone in the first 5 μm away from the lacunar wall was ~13% lower than the modulus of bone 16-20 μm from the lacuna. The decrease in modulus for perilacunar from non-perilacunar bone was less with OVX (~6%) and varied for OVX-treatment groups (3-11%). In a later study, Taylor *et al* studied the same bone samples, but different individual lacunae, and collected 20-μm linear profiles (1 μm spacing) using Raman spectroscopy.[79] For data pooled across all groups, there were small (≤ |2|%) but significant increases in mineral:matrix and collagen maturity and decreases in crystallinity and carbonate:phosphate for perilacunar compared with non-perilacunar bone. There may be several reasons for the greater changes in modulus, as opposed to tissue composition, for perilacunar versus non-perilacunar bone. Nanoindentation modulus of bone is affected by mineral content and mineral/matrix maturity but also the nanoporosity and organization of the bone tissue composite.[83,84]

The 'osteocytic osteolysis' phenotype is sometimes associated with a larger region of lower bone modulus near the LCS. Lane and coworkers found that glucocorticoid treatment lowered nanoindentation

modulus by ~40% in the hypomineralization 'halos'.[39] Kaya *et al* found that modulus from microindentation was 10-13% lower, depending on cortical location, for lactating versus control mice.[28] The authors attributed the variation in modulus to increased microporosity in lactation as opposed to changes in mineralization. Importantly, microindentation creates much larger indents than nanoindentation, and thus averages bone material properties over a larger volume. Differences in perilacunar bone mechanical properties for the 'aging' phenotype are not yet determined.

The mechanical properties of bone tissue near the LCS may impact whole-bone material properties. Stern *et al*[71] found that ultimate stress, work to failure, yield stress, and elastic modulus of the whole bone were modestly but significantly negatively correlated to the elastic modulus of perilacunar bone, but not non-perilacunar bone matrix, for OVX rats receiving sequential osteoporosis treatments. Importantly, it is not known if these treatments affected LCS remodeling activity or osteocyte viability. The heterogeneity of bone near osteocytes could also impact whole-bone fracture resistance. Tai and colleagues, using nanoscale bone mechanical property maps collected from AFM as inputs to FE models, proposed that bone's nanoscale heterogeneity allows for energy dissipation and could inhibit crack propagation.[85] In support of these ideas, the AFM study from Zhang and coworkers[82] found that the mechanical heterogeneity and also average dissipated energy were both higher in perilacunar and pericanalicular bone compared with bone farther away. However, the influence of LCS remodeling frequency and peri-LCS material properties on whole-bone fracture resistance is not yet determined.

1.6 Influence of altered LCS remodeling on strain experienced by the osteocyte

Changes to lacunar morphologies may influence the applied mechanical strain to the osteocyte environment. McCreadie *et al* performed a finite element (FE) analysis on two different-shaped lacunae with 12.0 mm×6.8 mm×5.8 mm and 17.4 mm×4.8 mm×3.8 mm dimensions for an applied triaxial strain resembling a physiological load in trabeculae.[86] The lacuna with greater aspect ratio experienced higher maximum principal strains along the lacunae major axis. These strains (up to about 10,000 μstain along the perilacunar bone major axis, but less than 2000 μstain for the osteocyte) would be classified as 'overload' from in vivo movement studies, demonstrating that the osteocyte may experience very different loading than the overall bone tissue environment.[87] In a different study, an FE model of an ellipsoid osteocyte lacuna interconnected with cylindrical channels representing groups of canaliculi was developed to examine how the dimensions of lacunar axes impact surrounding tissue strains.[88] A compressive load representative of walking was applied to a simulated whole femur. When the major lacunar axis increased from 10 μm to 20 μm, a 3.50% increase of the maximum compressive strain (~10,000 μstrain) was found at sites where these canaliculi meets the lacuna. In this study, the anisotropy ratio and dimensions of canaliculi remained constant between models. Prendergast and coworkers

reported that lacunae perpendicular to a tensile load experienced greater strain than those parallel to the load.[89] Taken together, these studies imply that lacunar size and shape may affect mechanical sensitivity because of higher received strains at the osteocyte. Further, applying loads from a novel direction could induce greater bone adaptation because of the higher strains engendered.

The contrast between perilacunar and non-perilacunar bone moduli may also influence strains experienced by the osteocyte, separately from the effects of changing lacunar size. Stern *et al* measured perilacunar and non-perilacunar bone moduli for OVX mice treated with various sequences of osteoporosis treatments or sham controls, and then utilized FEA to assess the impact of perilacunar modulus on lacunar strain.[71] The highest strains were found for sham mice, which also had the highest contrast between perilacunar and bone matrix moduli.. In another study, Bonivtch (Stern) and coworkers[72] used an FE model with variations in canalicular diameter, perilacunar modulus, and size of the perilacunar zone. They found that a lower perilacunar tissue modulus and increased canalicular diameter both increased strain at the canalicular-lacunar insertion. For a decrease in perilacunar modulus of 15% and 40% (taken as examples from the study's modulus-strain curves), the tissue strain increased by ~5% and ~15%, respectively. These relationships were independent of the size of the perilacunar zone and minimally influenced by the canalicular diameter. Changes in perilacunar tissue strains may affect how osteocytes sense their external environment and regulate the activities of osteoblasts and osteoclasts.[1,3,90] Taken together, these FE models suggest that lacunar size, shape, and orientation have modest influence on the strain experienced by osteocytes and that perilacunar modulus may have a greater impact. Changes to osteocyte strain would be expected to affect osteocyte mechanosensitivity and the coordination of osteoblasts and osteoclasts.[91]

2. Choosing tools to study LCS bone quality

The focus of this section is on techniques with microscale or sub-microscale resolution appropriate for resolve changes to bone tissue local to the LCS (**Table 2**). Tools that require synchrotron radiation, which delivers high-resolution imaging of bone structure and mineralization [27,61,76,92] but is limited to very few researchers, are reviewed briefly here and thoroughly elsewhere.[93–96]

2.1 Chemistry and composition

2.1.1 Raman spectroscopy

In Raman spectroscopy, molecules within the specimen are excited by the incident monochromatic laser light. While the majority of photons elastically scatter from the sample and return to the detector with no change in energy, a small fraction of the light (~1 in 10^7 photons) inelastically scatters off of the sample and either gains or loses energy.[97] The wavelength differences between the scattered and incident light correspond with specific molecular vibrations, leading to characteristic frequency shifts in the

Raman spectrum.[98] Raman spectroscopy is appropriate for the surface analysis of bulk samples and thus does not require preparing transparent sections.

Raman spectroscopy produces a bone 'signature' that can be studied for characteristics of bone mineral, collagen, and noncollagenous proteins. The bone mineral phase is primarily monitored through phosphate vibrations, including symmetric stretching of the phosphate to oxygen (P-O) bonds (v_1 PO_4), doubly degenerate O-P-O bending (v_2 PO_4), asymmetric P-O stretching (v_3 PO_4), and triply degenerate O-P-O bending (v_1 PO_4). Meanwhile, carbonate is present within the hydroxyapatite lattice as substitutions, including A type (carbonate substitution in hydroxide site) and B type (carbonate substitution in phosphate sites). [81,98–100] The carbonate measured at ~1070 cm^{-1} by Raman spectroscopy is B-type.[81] Collagen is monitored through amide I, amide II and amide III bands, as well as proline, hydroxyproline, and phenylalanine. The CH_2 band is associated with collagen side chains but also noncollagenous proteins. [98–100]

Raman measurements are usually provided in peak ratios, due to the sensitivity of the technique to surface roughness and height. Mineral to matrix ratio is assessed from ratios of the phosphate and collagen bands. While the v_1PO_4 and amide I bands have the greatest signal intensity, these bands have a major polarization mismatch and thus their relative intensities depend on sample orientation.[101] Several other ratios, including v_1PO_4:proline and v_2 PO_4:amide III have minimal polarization sensitivity and are often better choices.[101,102] The degree of carbonate substitution is usually measured as carbonate to v_1PO_4 ratio.[98] Crystallinity, shown to correlate with the mineral c-axis length from XRD, is measured as the inverse of the full-width at half maximum intensity of the v_1PO_4 band.[103] Each of these ratios can be measured from intensities or areas, for hydrated and dehydrated specimens. It is typical to subtract the contributions of embedding media (e.g., PMMA) from Raman spectra, and various protocols exist to subtract background fluorescence.[98–100]

Raman spectroscopy achieves microscale lateral and depth resolution. The depth resolution is a function of sample refractive index, incident wavelength, and microscope numerical aperture. A relationship between depth resolution and these parameters was estimated by Juang et al[104] as in Equation 1:

$$\Delta z = \pm \frac{4.4\lambda n}{2\pi(NA)^2} \quad \text{Equation 1}$$

Where Δz is the depth of focus that measures the tolerance of placement of the image plane in relation to the lens, NA is the numerical aperture of the objective lens, n is the refractive index of the immersion medium, and λ is the wavelength of the light. For a NA of 0.75, a wavelength of 785 nm, and an estimated refractive index of bone tissue set to 1.56, the estimated depth for bone would be around 1.5 μm.[105,106]

The lateral resolution for Raman microscopy is given by Equation 2:[101]

$$\Delta x = \frac{0.61\lambda(laser)}{NA} \quad \text{Equation 2}$$

where Δx is the radius of lateral resolution. For a NA of 0.75 and a wavelength of 785 nm, the estimated lateral resolution for bone would be ~0.6 μm. Both lateral and depth estimates represent 'best case resolutions' which are, in reality, greater because of sample roughness.

Raman spectroscopy has appropriate resolution to detect tissue maturation in the days to weeks after osteoid deposition in cortical rat bone.[31] Thus, it is compelling to consider how Raman spectroscopy can also yield information about the tissue maturity local to the LCS. However, several challenges limit this approach. First, tissue remodeling may be limited to the first micrometer from a lacuna, which competes with the resolution limit of this technique.[98,99] Next, while mineral:matrix ratio would be expected to change with tissue maturation, simultaneous changes to both the mineral and collagen phases local to the LCS can reduce the 'signal' of this biological effect (i.e., ratio stays close to constant despite changing numerator and denominator).

2.1.1. Fourier transform infrared spectroscopy

In FTIR measurement of bone, transmitted light excites the bond vibrations of bone tissue. The characteristic wavelength of these excited vibrations corresponds to the IR absorption peaks. It is required to study thin (2–5 μm) transparent sections. Common outcomes include mineral to matrix ratio, carbonate to phosphate ratio, crystallinity (mineral size and perfection), and collagen crosslinking maturity. However, the lateral resolution of FTIR is 6-10 μm, which competes with the spatial dimensions of lacunae themselves.[100,107–109] For this reason, FTIR may be appropriate for surveying compositional properties of bone matrix as influenced by changes in LCS networks but is less appropriate for ascertaining gradients in bone composition local to individual features of these networks.

2.1.3 Scanning electron microscopy

In scanning electron microscopy, incident electrons interact with the bone sample surface to acquire either morphological or compositional images. Several types of imaging are available, probing different interactions between the incident electrons and the sample surface and delivering height and/or compositional data at a range of spatial resolutions spanning many orders of magnitude.

Secondary mode

Secondary electrons (SE) are generated when the incident electron beam interacts with and ejects weakly bound valence or conduction-band electrons in the sample due to inelastic scattering.[110] SE electrons have low kinetic energy, which is reduced further through energy loss while traveling through the material. Thus, secondary electrons that reach the detector are generated from the top few nanometers from the

surface of the bone tissue. SE imaging yields topographic contrast to reveal morphologic features that can be used for measuring two-dimensional, nanoscale geometric information about the LCS, but not about bone mineral or matrix density. The finely focused beam produces excellent depth of field which provides for 3D representation of the imaged object. Secondary mode SEM can be complemented with acid etching to reveal canalicular attachments to osteocytes.[7,12,71]

Backscattered mode

Backscattered scanning electron microscopy (BSEM) provides compositional contrast, where mean atomic number elements are more efficient at generating backscattered electrons and thus appear brighter.[110] The backscatter coefficient, η, is the proportion of the incident electrons that return to the sample detector. The backscatter coefficient increases nonlinearly with increasing atomic number, Z, as described by Arnal *et al*[111,112] (Equation 3):

$$\eta = 2^{\frac{-9}{\sqrt{Z}}} \quad \text{Equation 3}$$

When measurement conditions are the same, a linear relationship is expected between grey level and backscattered coefficient[113], thus measured grey level from BSEM can be related to the effective Z for the bone tissue composite.

BSEM, when used qualitatively, provides definition between bone matrix and void spaces. Quantitative BSEM, usually referred to as either quantitative backscattered electron imaging (qBEI) or quantitative backscattered scanning electron microscopy (qBSE), delivers bone compositional data and is performed with the use of calibration materials. Reference standards of carbon and aluminum bracket the typical Z range of bone (9-13)[114] and are typically used to calibrate the sample grey levels.[35,80,115] Other reference standards, such as custom-made lithium borosilicate glasses, are less frequently used but can closely bracket the expected elemental density range of bone.[113,116]

qBEI and qBSE employ somewhat different approaches for measuring bone composition. In qBEI, the grey level of the sample as well as calibration standards are measured. Through setting the carbon and aluminum standards at specific grey levels (i.e., 25 and 225, respectively, for 8-bit images) the grey level of calibrated sample images can be related to weight percent calcium, where each grey level step represents an increase of 0.17% calcium.[80,115] A histogram of calcium weight percentages is generated from non-black pixels (which after calibration represent plastic or voids). The weighted average of this histogram is Ca_{Mean}. Ca_{Peak} is measured at the peak position of the histogram, the most frequently occurring value. Ca_{Width} is the full width at half maximum height of the histogram and represents heterogeneity of mineral content.[29,35,80,102,115,117,118] This method assumes that variation in grey level intensity is solely due to variation in calcium content and not other elements. The calcium weight percent measured from qBEI was found to have a strong correlation with v_2PO_4:amide III from Raman spectroscopy in human osteons.[102] Good correspondence is also seen with calcium weight percent

measured from SEM-EDS.[115] Meanwhile, in qBSE, the calibrated grey levels are related to a mineral volume fraction.[84,113,116,119,120] This mineral volume fraction is based on treating bone like a two-phase composite with organic and mineral phases of with given densities.[113]

Several considerations are important when using qBEI/qBSE for measurement of LCS bone tissue mineralization and quality. These techniques are able to monitor weight percentage of calcium, and thus provide an indication of tissue mineralization, but cannot measure collagen quantity or quality. qBEI/qBSE are also sensitive to a number of features that can affect the proportion of backscattered electrons arriving at the detector, including sample roughness, probe current and gain, and working distance, and thus care is required to assure low variance within and between imaging sessions. BSEM generally involves accelerating voltages of at least 10 kV (15-30 kV are common). As accelerating voltage decreases, charging effects increase as electrons concentrate near the sample surface. At very low accelerating voltages (< 2 kV), the relationship between atomic number and backscattered coefficient breaks down and the influence of the coatings and surface contamination on the backscattered coefficient can be problematic.[121,122] BSEM generally requires that nonconductive samples, such as bone, have a conductive coating (usually carbon). The resolution of BSEM depends on accelerating voltage. From Monte Carlo simulations, the most common interaction depth and radius of collectable BSEs for bone are ~0.5 and 1 μm at 15 kV and ~1 and 1.5 μm at 20 kV.[123] Thus, BSEM techniques, while having several advantages, do not have the required resolution for all questions involving bone composition local to the LCS.

Electron dispersive spectroscopy

Electron dispersive spectroscopy is a technique that can generate spot (~1 micron) elemental analyses or 2D elemental maps of sample surfaces by detecting characteristic secondary X-rays produced in the particle-beam interaction. When an incident electron interacts with an atom, a core electron is ejected and an outer electron fills the vacancy, releasing an x-ray with a wavelength that is proportional to the energy difference between the orbitals for that element. These x-rays occur at specific energy levels for each element; as a large number of atoms interact with the beam within the excitation volume, a spectrum of characteristic peaks is generated that that can serve to identify the elemental composition of the material.[110,124] The elemental resolution depends on the detector. Beryllium windows, which are now antiquated, cannot detect elements below sodium. Ultrathin polymer windows can detect lighter elements (including C, N, and O). However, detection efficiency is still low, as it is more difficult to ionize atoms for light elements. Modern silicon drift detectors, which do not require a window, offer improved detection of light elements.[125] SEM-EDS can deliver qualitative elemental maps or semi-quantitative measurement for spot analyses. Reliable semi-quantitative measurement requires studying flat samples

with low surface roughness (i.e., well-polished), and are improved through studying elemental reference standards with the same beam conditions.[124]

SEM-EDS has sometimes been used in bone research to study Ca/P ratios, where higher ratios may be associated with more mature bone.[7,126] SEM-EDS could be employed for elemental mapping of the LCS, but several considerations are important. First, while hydroxyapatite mineral would be readily mapped through monitoring calcium or phosphorus peaks, the ability to monitor the organic phase of bone depends on the instrument's detector and window. For systems capable of reliably monitoring light elements, nitrogen may be a better choice to monitor collagen than carbon. This is because carbon is present in hydroxyapatite, embedding materials, and surface contaminants. Second, because bone is insulating, a conductive coating is required. Third, SEM-EDS detectors are usually mounted at an angle. In the authors' experience, it is possible to observe 'shadowing' where the surface of a lacuna closer to the detector appears richer in the element of interest than the far surface. Rotating the sample and scanning the same area again can confirm whether or not this effect is happening. The lateral and depth resolution of SEM-EDS depends on accelerating voltage and material analyzed. From a Monte Carlo simulation performed by the authors of this Review using NIST DTSA II at 15 kV, x-ray emissions for calcium are generated within a volume with radius and depth dimension of ~2.5 μm each. For nitrogen, this volume has lateral radius of about ~2 μm and a depth of ~1 μm.[127] Thus, while SEM-EDS may be able to monitor density of both mineral and collagen matrix, it still may not be sensitive to bone compositional changes, especially for mineral, immediately adjacent to the LCS.

Auger electron spectroscopy

Auger electron spectroscopy (AES) is a technique commonly used in analytical surface characterization, but not yet commonly applied to mineralized tissues. When incident electrons interact with atoms, a core electron is ejected, and an outer electron fills the vacancy. The excess energy of this transition can be emitted as an x-ray (see SEM-EDS) or can be transferred to an outer electron, which is then emitted from the atom (i.e., Auger emission). While the sum electron yield of these two processes is unity, they do not have the same probability. Auger emission dominates for light elements, while the emission of x-rays increases with atomic number. While atomic ionization can happen beyond a micrometer of depth, Auger electrons have relatively low energy and thus their mean free paths are small. Thus, AES is limited to the first few nanometers of depth from the surface.[128]

AES is able to characterize elements characteristic of either bone mineral or matrix. The kinetic energy of the Auger emission is characteristic of the emitting atom. Because AES is a three-electron process, it is not able to identify H or He, but can identify all heavier elements. The AES detector is generally mounted coaxial to the electron beam, eliminating the shadowing effects that can interfere with

SEM-EDS of the LCS (note: such detector geometries are available but uncommon for EDS detectors). As with other SEM techniques, AES can be used to inventory elements present on a material surface in survey mode, it is possible for rastering scans to produce compositional maps of surfaces on a sub-micron scale, and ion beam sputtering procedures can be used to obtain compositional depth profiles into a material. Because Auger peaks are relatively small compared to background energy, it is common to analyze the first derivative of the spectra in order to identify elemental peaks, and published sensitivity factors can be used to determine sample surface composition.[128,129]

Several considerations need to be maintained for AES analysis of bone. First, because ultrahigh vacuum (10^{-9} torr) is required, PMMA or other off-gassing resins should be avoided, even if the resins are acceptable in conventional SEM techniques. Next, the sample should be thoroughly dehydrated. Third, insulating materials are challenging when using AES. Conductive coatings are not permissible because of the low interaction depth of the technique (i.e., the signal would only represent the coating). A number of strategies exist for studying insulating samples. These include tilting the sample, lowering the beam energy or current, neutralizing the surface with noble gas ions, or mounting thin sections on a conductive sample holder.[128] Another strategy is to coat the sample surface with a metal coating and either mask an area of interest or sputter off the coating with argon, or another inert gas, for a specific a region of interest. This same technique can be used to mill the surface for depth-profiling, but care should be taken to not preferentially etch atoms or introduce sample roughness.[128–130]

AES is only sparingly reported for bone[126,131,132]. A few studies employed AES to study calcium:phosphate ratio in bone pieces[131] or ground bone pellets[126,131], or mineralization and oxide formation of bone implant surfaces.[129,132] AES was able to distinguish osteoporotic bone from healthy bone as SEM-EDS at several skeletal sites for adult New Zealand White rabbits.[126] AES has also delivered elemental composition, including mineral and collagen components, for dental tissues.[130,133] To the best of our knowledge, AES has not been reported for studies of bone tissue surrounding the LCS. Although care needs to be taken to prepare appropriately smooth and dehydrated surfaces, AES does not require thin sections and, when performed properly, is not destructive. Thus, it is possible to pair AES and other techniques, such as atomic force microscopy, to generate complementary nanoscale maps of bone material properties near the LCS.

2.1.4 Transmission electron microscopy

Transmission electron microscopy (TEM) allows nanoscale resolution of bone morphology and mineralization. However, the technique requires bone tissue fixation, followed by the preparation of ultrathin sections.[134] TEM is useful for the study of mineralization of bone matrix around lacunae and canaliculi.[27] Bright field imaging yields images of mineral as well as collagen, while dark field imaging

delivers images that are dark except for where apatite scatters electrons from the 002 plane.[135] Thus, TEM can deliver crystal morphology and arrangement of crystals on collagen fibers.[134–137] TEM can also be used to identify crystal phase and thickness through diffraction-based techniques.[137,138] It is also possible to decalcify ultrathin sections to allow comparisons of mineralized and demineralized surfaces, which is useful for studying collagen characteristics.[134] However, TEM has a number of limitations. In addition to being particularly labor intensive to prepare, ultrathin sections are not suitable for nanomechanical assessment on the same regions due to both substrate and fixation effects.

2.1.5 High-resolution microcomputed tomography

The use of high-resolution microcomputed tomography (μCT) to monitor bone, including LCS network architecture, is the subject of several recent reviews[93–95] and is therefore discussed only briefly here. μCT allows for non-destructive three-dimensional analysis of internal bone tissue structure and mineralization.[93] Standard μCT does not achieve adequate resolution to visualize the LCS. Higher resolution μCT is now available as laboratory systems. These systems (e.g. Zeiss Xradia, Scanco 50, Bruker SkyScan 2214) can achieve submicroscale voxel resolution and have been used to image lacunae[41,139,140] and sometimes canaliculi.[141] Synchrotron-based CT systems (SRμCT) achieve higher resolution (50 nm to 150 nm[76,142,143]), which allows visualization of canaliculi[142] as well as measurement of microcracks.[144–146] When SRμCT is used in conjunction with XRD, mineral orientation can be estimated.[147] When used with SAXS, mineral shape, orientation, and quantity are accessible.[77,148–150] Ptychographic x-ray μCT is another technique relevant to LCS measurements.[96,151,152] Multiple high-resolution interference patterns are produced by scanning the specimen at several offset locations. These interference patterns are overlapped and then processed to reconstruct the 3D refractive index distribution of the specimen. This allows for quantitative volumetric mapping of both real (phase change) and imaginary (absorption) components of the reflective index. Using this approach, ptychographic x-ray tomography can achieve resolution (16-44 nm[153,154]) and contrast great enough to estimate nanoscale bone density variations of ~0.2%.[151]

2.2 Mechanical properties of bone tissue

2.2.1 Nanoindentation

Nanoindentation is a technique for microscale assessment of mechanical properties. This instrumented indentation technique utilizes a diamond tip that presses into the sample surface as displacement is recorded.[155] Tip actuators are either electrostatic or electromagnetic and allow either driving either a load-control or displacement-control indentation. Most nanoindentation tips are machined from diamond. Pyramidal (i.e., Berkovich) and conicospherical geometries are most common. While a

sharp, unworn Berkovich tip has an apical radius of ~125 nm, most indentations in bone are placed to depths of 300 nm – 1 micrometer and thus engage contact radii of 1-2 micrometers. Indentation plastic zones are assumed to extend to 1.5 times the contact radius for bone, and thus consecutive indents are usually spaced a minimum of 3 times the contact radius.[156,157] The lower limit of lateral and depth resolution is also influenced by the indenter noise floor and the sample surface roughness.[158]

In nanoindentation, typical measurements include modulus and hardness. Assuming elastic-plastic contact (a reasonable assumption for PMMA-embedded bone), the unloading curve is assumed to represent primarily elastic behavior. Thus, the stiffness is measured from a tangent line taken near the beginning of unloading. Stiffness is converted to modulus through measuring the tip contact area. Unlike traditional hardness testing, where residual tip areas are measured optically, nanoindentation tip areas are too small to efficiently measure directly. Instead, the tip is calibrated with respect to contact depth on reference standards (e.g., fused quartz), and contact depth is measured as a function of maximum depth.[155,159] Nanoindentation hardness is measured from the peak load divided by the contact area. Because elasticity is not neglected, nanoindentation hardness differs from conventional hardness testing for materials that are not perfectly plastic.[160] Measurement of time-dependent material properties through either performing creep or stress-relaxation tests or using dynamic nanoindentation are also well-developed for bone.[83,155,161,162] Most nanoindentation systems are capable of time-efficient two-dimensional mapping. Correlative work has also been used, where site-matched nanoindentation and either Raman spectroscopy or qBSE/qBEI allow correlation of composition and mechanical properties.[31,34,52,116,156]

2.2.2 Atomic Force Microscopy

Atomic force microscopy (AFM) is a technique that utilizes a tip with specified geometry attached to the end of a cantilever of known stiffness to provide nanoscale-resolution maps of material morphology and modulus. Features as small as canaliculi can be accurately mapped.[82] A stiff tip (e.g., silicon nitride) is attached to a cantilever, which can interact with the sample in various contact (i.e., dragging) or tapping type modes in raster scans of the material. The deflection of the cantilever during contact with the sample is monitored through the reflection of the laser off of the cantilever and onto a photodiode. AFM can be used to calculate sample modulus. Indentations can be applied to the material to generate force-distance curve. The force is calculated assuming that the cantilever behaves as a Hookean spring (Force = k*deflection), where k is the cantilever spring constant. From each curve, the modulus is calculated from the Hertzian contact model or variations upon it (e.g., adjusting for adhesion with models such as the Derjaguin-Muller-Toporov).[163] The position of the tip when it engages with the sample surface is also calculated and stored. This allows for sample topography to be determined simultaneously with modulus. Material properties can also be calculated through contact resonance AFM, where the tip is oscillated

through a range of frequencies in contact with the sample. The contact and free (i.e., not touching the sample) resonant frequencies are used to calculate sample material properties, including modulus.[157]

Several considerations should be maintained for reliable AFM stiffness mapping. Relatively high stiffness tips need to be used to obtain reliable data on stiff materials, such as bone.[157] These tips are typically more expensive and more difficult to tune due to their relatively high fundamental frequency. They also tend to wear quickly, which necessitates frequently calibrating the tip to ensure accurate measurement data. Despite these challenges, AFM is a promising way to study bone topology and material properties on the nanometer length scale and can be employed to study a variety of questions surrounding the osteocyte (**Figure 3**).

3. Key questions and future directions

Substantial evidence supports that osteocytes can resorb and replace tissue local to the lacunar-canalicular system (LCS) but we do not yet fully understand the reasons for, or repercussions of, LCS remodeling (**Table 3**). It is not contentious that the LCS participates in calcium homeostasis, but participation in phosphate homeostasis is less certain. Evidence also points towards the LCS having a role in bone tissue mineralization during health, and this begets additional questions about the role of the LCS at different stages of bone tissue maturation.

There is not a simple relationship between LCS remodeling and bone health, as there are at least two separate phenotype that occur throughout physiological and disease models. The ‘aging’ phenotype, in which osteocytes are less viable and LCS network architecture is contracted, and the ‘osteocytic osteolysis’ phenotype, in which LCS networks are enlarged. While the ‘aging’ phenotype appears to be maladaptive (i.e., more clearly associated with osteocyte dysfunction), ‘osteocytic osteolysis’ is probably adaptive on some occasions and maladaptive on others. In lactation, for example, liberation of mineral is adaptive, but in glucocorticoid therapy, larger lacunae and hypomineralization are not obviously helpful to the organism.

The essential question is whether and how LCS remodeling affects bone fracture resistance. A major current limitation is the lack of understanding of how tissue toughening mechanisms are affected by LCS remodeling. It is not sufficiently understood whether tissue composition and mechanical properties vary between remodeling and non-remodeling lacunae and canaliculi in health and in disease, as well as which of these changes are significant for bone mechanics. Work is needed across the lifespan and across disease models to understand the impacts of LCS remodeling on whole bone fracture resistance.

Moving forward, it is essential to employ the right tools to investigate the impacts of LCS remodeling on bone quality. One challenge is that many bone characterization techniques involve

microscale-or-greater resolution, while bone composition often varies at the nano-submicroscale near lacunae and canaliculi. It is important to not fall victim to ‘false negatives’ because of low resolution measurements. As an analogue, for several years, it was unclear if osteocyte lacunar morphologies change in aging. Multiple groups now show that lacunae indeed become smaller and more spherical with aging, but witnessing these changes required 3D visualization (as opposed to 2D). We expect that high-resolution mapping of bone composition and mechanical properties near osteocytes will yield insights that are not apparent with lower-resolution techniques. These careful efforts are needed for unraveling the possible roles of the osteocyte in bone quality maintenance and for identifying whether this most-abundant bone cell could be a compelling new target for preventing bone fracture.

Acknowledgements: This work was supported by the Department of Mechanical & Industrial Engineering and College of Engineering at Montana State University. We are grateful for helpful discussions with Nathaniel Rieders and Dr. David Mogk at the Montana State University Imaging and Chemical Analysis Laboratory. Research reported in this publication was supported by the National Institute of General Medical Sciences of the National Institutes of Health under Award Number P20GM103474. The content is solely the responsibility of the authors and does not necessarily represent the official views of the National Institutes of Health.

Table 1: LCS properties with different physiological and disease conditions

Physiological condition	Experimental model and skeletal sites	Changes to osteocyte viability	Changes to LCS morphology	Peri-LCS tissue composition & mineralization	Peri-LCS mechanical properties
Mineral homeostasis					
Lactation	C57Bl/6 mice *14-20 week females[28], midshaft femur.* *3-5 month females[38], fibula.*		*Lactation vs control or 1 week post weaning* ↑ lacunar area[28] *Lactation vs virgin control* ↑ lacunar volume[38]	*Lactation vs control or 1 week post weaning* ↓ carbonate:phosphate ratio[28] No changes in mineral:matrix ratio[28]	*Lactation vs control* ↓ elastic modulus for bone tissue with greater canalicular density[28]
	CD1 mice[9] *12 weeks before pregancy and weaning, multiple skeletal sites.*		*Lactation vs control or 1 week post weaning* ↑ lacunar area for cortical and trabecular tibiae, cortical lumbar vertebrae, but not calvaria		
	NMRI mice[44] *10-19 week females, cortical tibia.*		*Lactation vs control or 28 days post weaning* No changes in lacunar area		
PTH	Wistar rats[14] *8 months of age (sex not stated)* *4 week PTH treatment. Cortical tibia.*		*PTH(1,34)-treated continuously vs vehicle:* ↑ lacunar area		
	C57Bl/6J mice[48] *16 week males* *3 week treatment, cortical tibia*		*Intermittent PTH(1,34) treatment vs saline vehicle:* ↑ lacunar area	*Perilacunar vs. non-lacunar region PTH(1,34)-treated groups:* ↓ mineral:matrix ratio	

X-linked hypophosphatemia	C57BL/6J mice[50] *75 day females and males, cortical tibia*		*Hyp vs WT:* ↑ lacunar volume, surface area, lacunar number density ↓ canalicular number density and branching		
Chronic kidney disease (CKD)	Human iliac crest[51] *Men and women, mean age 56*		*High turnover vs low turnover CKD:* No changes in lacunar area. ↑ Lacunar number density, lacunar perimeter, lacunar porosity.		
Bisphosphonate and glucocorticoid treatments					
Bisphosphonate-related osteonecrosis (BRONJ)	Human jawbone[76] *BRONJ or healthy controls; females and male adults.*			*BRONJ vs controls:* ↓ mineral gradient from LCS wall to adjacent bone tissue.	
Glucocorticoid treatment (GC)	Swiss-Webster mice[39] *6 month males 21 days of prednisolone treatment or placebo. Lumbar vertebra.*	*GC treatment vs placebo:* ↑ osteocyte apoptosis	*GC treatment vs placebo:* ↑ lacunar area	*GC treatment, perilacunar vs non-perilacunar bone:* ↓ mineral:matrix ratio	*GC treatment, perilacunar vs non-perilacunar bone:* ↓ elastic modulus
Sex hormones and osteoporosis					
Ovariectomy (OVX)	Swiss-Webster mice[39] *6 month females, 21 days post OVX or Sham surgeries. Lumbar vertebra.*	*OVX vs Sham:* No difference in osteocyte apoptosis	*OVX vs Sham:* ↑ lacunar area	*OVX vs Sham treatment, perilacunar vs non-perilacunar bone* No changes in mineral:matrix ratio	*OVX vs Sham treatment, perilacunar vs non-perilacunar bone*

					No changes in elastic modulus
	Sprague-Dawley rats[70] *20 week females* *6 weeks post-OVX or Sham surgeries.* *Proximal tibia.*		*OVX vs Sham:* ↑lacunar-canalicular porosity and canalicular volume at metaphysis. No changes in lacunar volume or lacunar number density.		
	Sprague-Dawley rats *6 month females* *8 week post-OVX* *270 days of different sequences of osteoporosis treatments*[71,79]*Cortical tibia.*		*OVX & OVX-treatment groups vs Sham:* No difference in lacunar size or lacunar number density[71]	*Perilacunar vs non-lacunar regions for pooled samples across groups:* ↓ carbonate:phosphate ratio ↑ mineral:matrix ratio ↑ collagen maturity ↓ crystallinity[79]	*Perilacunar vs. non-lacunar regions for pooled samples:* ↓ elastic modulus[71] *OVX & OVX-treatment groups vs sham:* ↓ elastic modulus contrast for perilacunar vs non-perilacunar region[71]
Unloading					
Sciatic neurectomy	Sprague Dawley rats[18] *30 week females; sciatic neurectomy at 3 weeks. Cortical tibia.*		*Sciatic neurectomy vs control:* ↓ lacunar volume ↓ lacunar number density		
Hindlimb unloading	Sprague Dawley rats[19] *28 week males* *HLU via tail suspension for 28 days. Distal femur.*	*HLU vs control:* ↑ osteocyte apoptosis ↓ occupied lacunae	*HLU vs control:* ↓ lacunar number density		
Spaceflight	C57Bl/6N mice[17]	*Flight vs control:*	*Flight vs control:*		

	23 week males *1 month of flight, cortical femur.*	↑ fraction of empty lacunae	↓ lacunar volume:total volume (medial zone only) ↓ lacunar volume (posterior zone only) ↑ sphericity of lacunae (posterior zone only)		
	C57Bl/6 mice[62] *16 week females* *15 days of flight, ischia*	*Flight vs control:* No changes in empty lacunae	*Flight vs control:* ↑ lacunar area and perimeter ↓ sphericity of lacunae ↑ canalicular diameter No changes in lacunar number density		
Botox	Wistar rats[61] *14 week females, 28 week period post-injection, cortical femur.*		*Botox vs contralateral or external control:* No changes in lacunar size or number density over 28 weeks post-injection		
Exercise					
Aerobic exercise	C57Bl/6 mice[49] *16 week males* *30 min of running for 21 days, cortical tibia.*		No changes in lacunar area	*Perilacunar vs. non-lacunar region in exercise group:* ↑ carbonate:phosphate ratio ↓ mineral:matrix ratio	
	Zebrafish[65] *4.5 month old* *4 weeks of exercise in a swim tunnel. Vertebrae.*		No changes in lacunar volume and sphericity		
Aging					
Mouse models	C57Bl/6 mice[16] *5, 22-23 month females and males. Cortical femur.*	*With increase in age:* ↓ osteocyte cell volume ↓ fraction of empty lacunae in females	*With increase in age:* ↓ lacunar volume in distal but not midshaft femur, *in males* ↓ lacunar number density ↓ canalicular and dendrite number		
	C57Bl/6 mice[15,52]		*With increase in age:*		

	6, 18, 24 month males. Cortical tibia.		↓ lacunar area and volume ↓ lacunar number density ↑ sphericity of lacunae		
	C57BL/6JRccHsd mice[37] *5, 23 month females. Fibula.*		*With increase in age:* ↓ lacunar volume ↑ sphericity of lacunae		
Human models	Human cortical femur[53] *10-90 year old females and males.*		*With increase in age:* ↓ lacunar number density	*With increase in age:* ↑ number of highly mineralized lacunae	
	Human cortical femur[54] *16-73 years. Females and males. Cortical femur.*		*With increase in age:* ↓ lacunar number density		
	Human iliac crest bone[55] *Females and males, mean age 57 years*	*For >55 years years vs <55 years* ↓ Osteocyte number density No changes in fraction of empty lacunae	*For >55 years vs <55 years* ↓ lacunar number density No change in lacunar area		
	Human iliac crest bone[56] *19-97 year old females and males*		*With increase in age:* No changes in lacunar volume ↓ lacunar number density		
	Human femur cortical bone[57] *20-86 year females*		*With increase in age:* ↓ lacunar volume ↓ sphericity of lacunae		

Table 2: Tools for assessing peri-LCS bone quality

Technique	Resolution	Advantages	Limitations	References *use of technique for LCS analysis # General reference papers
Vibrational spectroscopy				
Raman spectroscopy	Lateral: 0.6 -1 µm Depth: 1.5 µm	• Sensitive to bone mineral density as well as mineral and matrix maturity. • Hydrated, dehydrated, and embedded samples can all be studied. • Not limited to transparent samples.	• Changing mineral:matrix ratio may result from either altered mineral, matrix, or bone. • Large maps are time intensive.	28,39,48,49,79* 98–100#
Fourier-transform infrared spectroscopy (FTIR)	Lateral: 6-10 µm. Depth: 2-5 µm (thickness of transparent thin sections).	• Sensitive to bone mineral density as well as mineral and matrix maturity. • High signal:noise ratio.	• Transparent sections required. • Resolution is low compared with LCS dimensions. • Significant interference from water; embedded samples required.	100,108,164#
Electron microscopy				
Secondary mode SEM	Lateral and depth: As low as ~10 nm for field-emission SEM	• Possible to image lacunar and canalicular geometries. Acid-etching aids the visualization of canaliculi. • Low accelerating voltages can be used.	• High vacuum generally required for high magnifications. • Metal surface coating typically required for bone.	7,12,165,166* 110#
Backscattered SEM (BSEM) and quantitative backscattered electron imaging (qBEI)	Lateral: ~0.4 µm at 15kV Depth: ~ 0.9 µm at 15 kV	• Displays compositional contrast. • Rapid mapping possible. • High contrast between bone tissue and LCS features. • Can deliver %Ca or mineral volume fraction when reference standards are used appropriately.	• Not sensitive to bone matrix. • Samples need carbon coating. • Low accelerating voltages not possible for quantitative work; limits resolution.	BSEM: 12,20,24,26,28,44,166* qBEI: 7,49,73,167*
SEM-electron dispersive	Lateral: 0.5-2.5 µm	• Detects mineral content (Ca and P maps).	• Older detectors cannot detect matrix elements.	49,126* 125,168#

spectroscopy (SEM-EDX)	Depth: 0.5-1 μm	• Samples can also be imaged with other SE or BSE.	• Shadowing effect from detector angle.	
Transmission electron microscopy (TEM)	Lateral: < 1 nm Depth: 50-100 nm	• Can measure lacunar and canalicular ultrastructure • Can measure mineral size, shape, and phase. • Demineralized samples can be assessed for collagen orientation.	• Sample fixation necessary. • Ultrathin samples required.	27,166,169∗ 134–137#
High resolution 3D imaging				
High-resolution computed tomography (μCT) (commercially-available lab systems)	Pixel: 0.6-2 μm	• Non-destructive 3D imaging. • Can measure lacunae and sometimes canaliculi.	• Beam hardening artifacts. • Insufficient spatial resolution for some structural questions.	41,139–141∗ 95#
Synchrotron-radiation (SR-μCT)	Pixel: 50 nm-150 nm	In addition to μCT advantages: • Resolution allows detection of canaliculi and microcracks. • No beam hardening artifact. • When combined with SAXS/XRD can measure crystal orientation, size, and distribution.	• Limited access. • Complex additional instruments. • High radiation rate.	27,61,76,92,142–146,170–177∗ 93–95#
Ptychographic x-ray μCT	Pixel: 16-44 nm	• Higher resolution than SR-μCT. • The resolution does not depend on the lens (only wavelength limited).	• Similar limitations as SR-μCT.	151,153,154∗ 94,96,151,153,178,179#
Tissue-scale indentation				
Atomic force microscopy (AFM)	Lateral: ~20 nm Depth: ~20 nm	• Hydrated, dehydrated, and embedded samples can all be imaged. • Sufficient resolution to determine modulus for nanoscale LCS structural features. • LCS geometries can also be measured.	• Difficult to image high modulus materials. • Requires fine surface polish. • Depth of topographic features accuracy dependent on adjacent surface features and sample roughness. • Time intensive.	82,180∗ 156,157,163#

			• Tips are fragile and wear quickly. • Requires frequent tip calibration.	
Nanoindentation	Lateral: > 1 μm Depth: > 100s of nm – 1 μm	• Capable of mapping relatively large regions (100+ μm). • Diamond tips less prone to wear. • Designed for stiff substrates.	• Resolution is not well matched for gradation around canaliculi. • Requires fine surface polish. • Time intensive • Requires tip area calibration.	39,70,71,82* 83,155#

Papers of particular interest:

- Of importance

- Nango, N. *et al.* Osteocyte-directed bone demineralization along canaliculi. *Bone* **84**, 279–288 (2016)
  This paper demonstrates that mineral density was lowest in the hundreds of nanometers around LCS and gradually increased within the first 2 micrometers in mice.

- Hesse, B. *et al.* Canalicular network morphology is the major determinant of the spatial distribution of mass density in human bone tissue: Evidence by means of synchrotron radiation phase-contrast nano-CT. *J. Bone Miner. Res.* **30**, 346–356 (2015). 10.1002/jbmr.2324
  This study demonstrates that mass density in the direct vicinity of the LCN of human jaw bone is different from the mean mass density of the bone tissue, resulting in mass density gradients with respect to both the lacunar and the canalicular boundaries.

- Zhang, S., Bach-gansmo, F. L., Xia, D., Besenbacher, F. & Birkedal, H. Nanostructure and mechanical property of the osteocyte lacunar-canalicular network associated bone matrix revealed by quantitative nanomechanical mapping. (2015). doi:10.1007/s12274-015-0825-8 10.1007/s12274-015-0825-8
  This paper reveals lower and more variable moduli in the immediate vicinity of the lacunae in rats. The modulus of peri-canalicular bone is also lower adjacent to canaliculi but differs with distance down the canaliculus from the lacunar wall.

- Kaya, S. *et al.* Lactation-induced changes in the volume of osteocyte lacunar-canalicular space alter mechanical properties in cortical bone tissue. *J. Bone Miner. Res.* **32**, 688–697 (2017). PMC5395324
  This paper demonstrates mineral gradients around canaliculi in lactating and non-lactating mice. The paper also demonstrates that lower modulus in the bone of lactating mice may be attributed to increased lacunar-canalicular porosity.

- Lane, N. E. *et al.* Glucocorticoid-Treated Mice Have Localized Changes in Trabecular Bone Material Properties and Osteocyte Lacunar Size That Are Not Observed in Placebo-Treated or Estrogen-Deficient Mice. *J. Bone Miner. Res.* **21**, 466–476 (2005).
  This study found reduced elastic modulus around the lacunae and a "halo" of hypomineralized bone surrounding the lacunae in GC-treated mice.

- Gardinier, J. D., Al-Omaishi, S., Morris, M. D. & Kohn, D. H. PTH signaling mediates perilacunar remodeling during exercise. *Matrix Biol.* **52**–**54**, 162–175 (2016). PMC4875803
  This paper demonstrates that bone composition around lacunae changes in exercise and that these changes are dependent on endogenous PTH activity.

- Qing, H. *et al.* Demonstration of osteocytic perilacunar/canalicular remodeling in mice during lactation. *J. Bone Miner. Res.* **27**, 1018–1029 (2012). 10.1002/jbmr.1567
  This work shows that osteocytes remove mineralized matrix through molecular mechanisms similar to those utilized by osteoclasts.

REFERENCES

1. Schaffler, M. B., Cheung, W. Y., Majeska, R. & Kennedy, O. Osteocytes: Master orchestrators of bone. *Calcif. Tissue Int.* **94**, 5–24 (2014).
2. Yee, C. S., Schurman, C. A., White, C. R. & Alliston, T. Investigating Osteocytic Perilacunar/Canalicular Remodeling. *Curr. Osteoporos. Rep.* **17**, 157–168 (2019).
3. Bonewald, L. F. The amazing osteocyte. *J. Bone Miner. Res.* **26**, 229–238 (2011).
4. Buenzli, P. R. & Sims, N. A. Quantifying the osteocyte network in the human skeleton. *Bone* **75**, 144–150 (2015).
5. Varga, P. *et al.* Synchrotron X-ray phase nano-tomography-based analysis of the lacunar–canalicular network morphology and its relation to the strains experienced by osteocytes in situ as predicted by case-specific finite element analysis. *Biomech. Model. Mechanobiol.* **14**, 267–282 (2015).
6. Beno, T., Yoon, Y. J., Cowin, S. C. & Fritton, S. P. Estimation of bone permeability using accurate microstructural measurements. *J. Biomech.* **39**, 2378–2387 (2006).
7. Milovanovic, P. *et al.* Osteocytic canalicular networks: Morphological implications for altered mechanosensitivity. *ACS Nano* **7**, 7542–7551 (2013).
8. Remaggi, F., Canè, V., Palumbo, C. & Ferretti, M. Histomorphometric study on the osteocyte lacuno-canalicular network in animals of different species. I. Woven-fibered and parallel-fibered bones. *Ital. J. Anat. Embryol. = Arch. Ital. di Anat. ed Embriol.* **103**, 145–155 (1998).
9. Qing, H. & Bonewald, L. F. Osteocyte remodeling of the perilacunar and pericanalicular matrix. *Int. J. Oral Sci.* **1**, 59–65 (2009).
10. Belanger, L. F. & Migicovsky, B. . Histochemical evidence of proteolysis in bone: the influence of parathormone. *J. Histochem. Cytochem.* **11**, 734–737 (1963).
11. Belanger, L. R. Osteocytic Osteolysis. *Calcif. Tissue Int.* **12**, 1–12 (1969).
12. Qing, H. *et al.* Demonstration of Osteocytic Perilacunar / Canalicular Remodeling During Lactation. *JBMR* **27**, 1018–1029 (2012).
13. Wysolmerski, J. J. Osteocytic osteolysis: time for a second look? *Bonekey Rep.* **1**, 229 (2012).
14. Tazawa, K. *et al.* Osteocytic osteolysis observed in rats to which parathyroid hormone was continuously administered. *JBMR* **22**, 524–529 (2004).
15. Heveran, C. M., Rauff, A., King, K. B., Carpenter, R. D. & Ferguson, V. L. A new open-source tool for measuring 3D osteocyte lacunar geometries from confocal laser scanning microscopy reveals age-related changes to lacunar size and shape in cortical mouse bone. *Bone* **110**, 115–127 (2018).
16. Tiede-Lewis, L. M. *et al.* Degeneration of the osteocyte network in the C57Bl/6 mouse model of aging. *Aging (Albany. NY).* **9**, 2190–2208 (2017).
17. Gerbaix, M. *et al.* One-month spaceflight compromises the bone mechanical properties, osteocyte survival and lacunae volume in mature mice skeletons. *Sci. Rep.* **7**, 2659 (2017).
18. Britz, H. M., Carter, Y., Jokihaara, J. & Leppanen, O. Prolonged unloading in growing rats reduces cortical osteocyte lacunar density and volume in the distal tibia. *Bone* **51**, 913–919 (2012).

19. Swift, J. M., Swift, S. N., Allen, M. R. & Bloomfield, S. A. Beta-1 Adrenergic Agonist Treatment Mitigates Negative Changes in Cancellous Bone Microarchitecture and Inhibits Osteocyte Apoptosis during Disuse. **9**, 1–8 (2014).

20. Jähn, K. *et al.* Osteocytes Acidify Their Microenvironment in Response to PTHrP In Vitro and in Lactating Mice In Vivo. *J. Bone Miner. Res.* **32**, 1761–1772 (2017).

21. Alemi, A. S. *et al.* Glucocorticoids cause mandibular bone fragility and suppress osteocyte perilacunar-canalicular remodeling. *Bone Reports* **9**, 145–153 (2018).

22. Fowler, T. W. *et al.* Glucocorticoid suppression of osteocyte perilacunar remodeling is associated with subchondral bone degeneration in osteonecrosis. *Sci. Rep.* **7**, 44618 (2017).

23. Dole, N. S. *et al.* Osteocyte-Intrinsic TGF-β Signaling Regulates Bone Quality through Perilacunar/Canalicular Remodeling. *Cell Rep.* **21**, 2585–2596 (2017).

24. Lotinun, S. *et al.* Cathepsin K-deficient osteocytes prevent lactation-induced bone loss and parathyroid hormone suppression. *J. Clin. Invest.* **130**, 3058–3071 (2019).

25. Sekita, A., Matsugaki, A., Ishimoto, T. & Nakano, T. Synchronous disruption of anisotropic arrangement of the osteocyte network and collagen/apatite in melanoma bone metastasis. *J. Struct. Biol.* **197**, 260–270 (2017).

26. Yajima, A. *et al.* Osteocytic perilacunar/canalicular turnover in hemodialysis patients with high and low serum PTH levels. *Bone* **113**, 68–76 (2018).

27. Nango, N. *et al.* Osteocyte-directed bone demineralization along canaliculi. *Bone* **84**, 279–288 (2016).

28. Kaya, S. *et al.* Lactation-induced changes in the volume of osteocyte lacunar-canalicular space alter mechanical properties in cortical bone tissue. *J. Bone Miner. Res.* **32**, 688–697 (2017).

29. Ruffoni, D., Fratzl, P., Roschger, P., Klaushofer, K. & Weinkamer, R. The bone mineralization density distribution as a fingerprint of the mineralization process. *Bone* **40**, 1308–1319 (2007).

30. Martin, B. Mathematical model for the mineralization of bone. *J. Orthop. Res.* **12**, 375–383 (1994).

31. Donnelly, E., Boskey, A. L., Baker, S. P. & Van Der Meulen, M. C. H. Effects of tissue age on bone tissue material composition and nanomechanical properties in the rat cortex. *J. Biomed. Mater. Res. - Part A* **92**, 1048–1056 (2010).

32. Boskey, A. L. Mineralization of Bones and Teeth. *Elements* **3**, 385–391 (2007).

33. Nyman, J. S. *et al.* Age-related effect on the concentration of collagen crosslinks in human osteonal and interstitial bone tissue. *Bone* **39**, 1210–1217 (2006).

34. Lloyd, A. A. *et al.* Atypical fracture with long-term bisphosphonate therapy is associated with altered cortical composition and reduced fracture resistance. *PNAS* **114**, (2017).

35. Roschger, P., Paschalis, E. P., Fratzl, P. & Klaushofer, K. Bone mineralization density distribution in health and disease. *Bone* **42**, 456–466 (2008).

36. Schaffler, M. B., Choi, K. & Milgrom, C. Aging and matrix microdamage accumulation in human compact bone. *Bone* **17**, 521–525 (1995).

37. Hemmatian, H. *et al.* Age-related changes in female mouse cortical bone microporosity. *Bone* **113**,

1–8 (2018).

38. Hemmatian, H. *et al.* Mechanical Loading Differentially Affects Osteocytes in Fibulae from Lactating Mice Compared to Osteocytes in Virgin Mice: Possible Role for Lacuna Size. *Calcif. Tissue Int.* **103**, 675–685 (2018).

39. Lane, N. E. *et al.* Glucocorticoid-Treated Mice Have Localized Changes in Trabecular Bone Material Properties and Osteocyte Lacunar Size That Are Not Observed in Placebo-Treated or Estrogen-Deficient Mice. *J. Bone Miner. Res.* **21**, 466–476 (2005).

40. Tang, S. Y., Herber, R. P., Ho, S. P. & Alliston, T. Matrix metalloproteinase-13 is required for osteocytic perilacunar remodeling and maintains bone fracture resistance. *J. Bone Miner. Res.* **27**, 1936–1950 (2012).

41. Kegelman, C. D. *et al.* YAP and TAZ Mediate Osteocyte Perilacunar/Canalicular Remodeling. *J. Bone Miner. Res.* **00**, 1–15 (2019).

42. Mazur, C. M. *et al.* Osteocyte dysfunction promotes osteoarthritis through MMP13-dependent suppression of subchondral bone homeostasis. *Bone Res.* 1–17 (2019).

43. Ritchie, R. O. *et al.* Measurement of the toughness of bone: A tutorial with special reference to small animal studies. *Bone* **43**, 798–812 (2008).

44. Wittig, N. K. *et al.* No Signature of Osteocytic Osteolysis in Cortical Bone from Lactating NMRI Mice. *Calcif. Tissue Int.* **105**, 308–315 (2019).

45. Boass, A., Garner, S. C., Schultz, V. L. & Toverud, S. U. Regulation of serum calcitriol by serum ionized calcium in rats during pregnancy and lactation. *J. Bone Miner. Res.* **12**, 909–914 (1997).

46. Knight, C. H., Maltz, E. & Docherty, A. H. Milk yield and composition in mice: Effects of litter size and lactation number. *Comp. Biochem. Physiol. -- Part A Physiol.* **84**, 127–133 (1986).

47. Speakman, J. R. The physiological costs of reproduction in small mammals. *Philos. Trans. R. Soc. B Biol. Sci.* **363**, 375–398 (2008).

48. Gardinier, J. D., Al-Omaishi, S., Rostami, N., Morris, M. D. & Kohn, D. H. Examining the influence of PTH(1-34) on tissue strength and composition. *Bone* **117**, 130–137 (2018).

49. Gardinier, J. D., Al-Omaishi, S., Morris, M. D. & Kohn, D. H. PTH signaling mediates perilacunar remodeling during exercise. *Matrix Biol.* **52**–**54**, 162–175 (2016).

50. Tokarz, D. *et al.* Hormonal regulation of osteocyte perilacunar and canalicular remodeling in the hyp mouse model of x-linked hypophosphatemia. *J. Bone Miner. Res.* **33**, 499–509 (2018).

51. Misof, B. M. *et al.* Bone matrix mineralization and osteocyte lacunae characteristics in patients with chronic kidney disease - mineral bone disorder (CKD-MBD). *J Musculoskelet Neuronal Interact* **19**, 196–206 (2019).

52. Heveran, C. M. *et al.* Chronic kidney disease and aging differentially diminish bone material and microarchitecture in C57Bl/6 mice. *Bone* **127**, 91–103 (2019).

53. Busse, B. *et al.* Decrease in the osteocyte lacunar density accompanied by hypermineralized lacunar occlusion reveals failure and delay of remodeling in aged human bone. *Aging Cell* **9**, 1065–1075 (2010).

54. Vashishth, D., Verborgt, O., Divine, G., Schaffler, M. B. & Fyhrie, D. P. Decline in osteocyte lacunar density in human cortical bone is associated with accumulation of microcracks with age.

Bone **26**, 375–380 (2000).

55. Mullender, M. G., Van Der Meer, D. D., Huiskes, R. & Lips, P. Osteocyte density changes in aging and osteoporosis. *Bone* **18**, 109–113 (1996).

56. Bach-Gansmo, F. L. *et al.* Osteocyte lacunar properties and cortical microstructure in human iliac crest as a function of age and sex. *Bone* **91**, 11–19 (2016).

57. Carter, Y., Thomas, C. D. L., Clement, J. G. & Cooper, D. M. L. Femoral osteocyte lacunar density, volume and morphology in women across the lifespan. *J. Struct. Biol.* **183**, 519–526 (2013).

58. Farr, J. *et al.* Identification of senescent cells in the bone microenvironment. *J. Bone Miner. Res.* **31**, 1920–1929 (2016).

59. Sherk, V. D. & Rosen, J. Senescent and apoptotic osteocytes and aging : Exercise to the rescue ? *Bone* **121**, 255–258 (2019).

60. Jilka, R. L., Noble, B. & Weinstein, R. S. Osteocyte apoptosis. *Bone* **54**, 264–271 (2013).

61. Bach-Gansmo, F. L., Wittig, N. K., Brüel, A., Thomsen, J. S. & Birkedal, H. Immobilization and long-term recovery results in large changes in bone structure and strength but no corresponding alterations of osteocyte lacunar properties. *Bone* **91**, 139–147 (2016).

62. Blaber, E. A. *et al.* Microgravity Induces Pelvic Bone Loss through Osteoclastic Activity, Osteocytic Osteolysis, and Osteoblastic Cell Cycle Inhibition by CDKN1a/p21. *PLoS One* **8**, (2013).

63. Kohrt, W. M. *et al.* Maintenance of Serum Ionized Calcium During Exercise Attenuates Parathyroid Hormone and Bone Resorption Responses. *J. Bone Miner. Res.* **33**, 1326–1334 (2018).

64. Kohrt, W. M. *et al.* Dermal calcium loss is not the primary determinant of parathyroid hormone secretion during exercise. *Med. Sci. Sports Exerc.* **51**, 2117–2124 (2019).

65. Suniaga, S., Rolvien, T., Scheidt, A., Fiedler, I. A. K. & Hrishikesh, A. Increased mechanical loading through controlled swimming exercise induces bone formation and mineralization in adult zebrafish. *Sci. Rep.* 1–13 (2018).

66. Sharma-Ghimire, P., Chen, Z., Sherk, V., Bemben, M. & Bemben, D. Sclerostin and parathyroid hormone responses to acute whole-body vibration and resistance exercise in young women. *J. Bone Miner. Metab.* **37**, 358–367 (2019).

67. Falk, B. *et al.* Differential sclerostin and parathyroid hormone response to exercise in boys and men. *Osteoporos. Int.* **27**, 1245–1249 (2016).

68. Tomkinson, A., Gevers, E. F., Wit, J. M., Reeve, J. & Noble, B. S. The Role of Estrogen in the Control of Rat Osteocyte Apoptosis. *JBMR* **13**, 1243–1250 (1998).

69. Follet, H. *et al.* Risedronate and alendronate suppress osteocyte apoptosis following cyclic fatigue loading. *Bone* **40**, 1172–1177 (2007).

70. Sharma, D. *et al.* Alterations in the osteocyte lacunar–canalicular microenvironment due to estrogen deficiency. *Bone* **51**, 488–497 (2012).

71. Stern, A. R. *et al.* Effect of osteoporosis treatment agents on the cortical bone osteocyte microenvironment in adult estrogen-deficient, osteopenic rats. *Bone Reports* **8**, 115–124 (2018).

72. Bonivtch, A. R., Bonewald, L. F. & Nicolella, D. P. Tissue strain amplification at the osteocyte lacuna : A microstructural finite element analysis. *J. Biomech.* **40**, 2199–2206 (2007).

73. Bach-Gansmo, F. L. *et al.* Osteocyte lacunar properties in rat cortical bone: Differences between lamellar and central bone. *J. Struct. Biol.* **191**, 59–67 (2015).

74. Ionova-Martin, S. S. *et al.* Reduced size-independent mechanical properties of cortical bone in high-fat diet-induced obesity. *Bone* **46**, 217–225 (2010).

75. Ionova-Martin, S. S. *et al.* Changes in cortical bone response to high-fat diet from adolescence to adulthood in mice. *Osteoporos. Int.* **22**, 2283–2293 (2011).

76. Hesse, B. *et al.* Canalicular network morphology is the major determinant of the spatial distribution of mass density in human bone tissue: Evidence by means of synchrotron radiation phase-contrast nano-CT. *J. Bone Miner. Res.* **30**, 346–356 (2015).

77. Kerschnitzki, M. *et al.* Architecture of the osteocyte network correlates with bone material quality. *J. Bone Miner. Res.* **28**, 1837–1845 (2013).

78. Nicolella, D. P. *et al.* Effects of nanomechanical bone tissue properties on bone tissue strain: Implications for osteocyte mechanotransduction. *J. Musculoskelet. Neuronal Interact.* **8**, 330–331 (2008).

79. Taylor, E. A. *et al.* Sequential Treatment of Estrogen Deficient, Osteopenic Rats with Alendronate, Parathyroid Hormone (1–34), or Raloxifene Alters Cortical Bone Mineral and Matrix Composition. *Calcif. Tissue Int.* **106**, 303–314 (2020).

80. Roschger, A. *et al.* The contribution of the pericanalicular matrix to mineral content in human osteonal bone. *Bone* **123**, 76–85 (2019).

81. Wopenka, B. & Pasteris, J. D. A mineralogical perspective on the apatite in bone. *Mater. Sci. Eng. C* **25**, 131–143 (2005).

82. Zhang, S. *et al.* Nanostructure and mechanical properties of the osteocyte lacunar-canalicular network-associated bone matrix revealed by quantitative nanomechanical mapping. *Nano Res.* **8**, 3250–3260 (2015).

83. Lewis, G. & Nyman, J. S. The use of nanoindentation for characterizing the properties of mineralized hard tissues: State-of-the art review. *J. Biomed. Mater. Res. - Part B Appl. Biomater.* **87**, 286–301 (2008).

84. Oyen, M. L., Ferguson, V. L., Bembey, A. K., Bushby, A. J. & Boyde, A. Composite bounds on the elastic modulus of bone. *J. Biomech.* **41**, 2585–2588 (2008).

85. Tai, K., Dao, M., Suresh, S., Palazoglu, A. & Ortiz, C. Nanoscale heterogeneity promotes energy dissipation in bone. *Nat. Mater.* **6**, 454–462 (2007).

86. McCreadie, B. R., Hollister, S. J., Schaffler, M. B. & Goldstein, S. A. Osteocyte lacuna size and shape in women with and without osteoporotic fracture. *J. Biomech.* **37**, 563–572 (2004).

87. Nazer, R. Al, Lanovaz, J., Kawalilak, C., Johnston, J. D. & Kontulainen, S. Direct in vivo strain measurements in human bone — A systematic literature review. *J. Biomech.* **45**, 27–40 (2012).

88. Apostolopoulos, C. A. & Deligianni, D. D. Prediction of local cellular deformation in bone - Influence of microstructure dimensions. *J. Musculoskelet. Neuronal Interact.* **9**, 99–108 (2009).

89. Prendergast, P. J. & Huiskes, R. Microdamage and osteocyte-lacuna strain in bone: A

microstructural finite element analysis. *J. Biomech. Eng.* **118**, 240–246 (1996).

90. Prideaux, M., Findlay, D. M. & Atkins, G. J. Osteocytes: The master cells in bone remodelling. *Curr. Opin. Pharmacol.* **28**, 24–30 (2016).

91. Hemmatian, H., Bakker, A. D., Klein-Nulend, J. & van Lenthe, G. H. Aging, Osteocytes, and Mechanotransduction. *Curr. Osteoporos. Rep.* **15**, 401–411 (2017).

92. Mader, K. S., Schneider, P., Müller, R. & Stampanoni, M. A quantitative framework for the 3D characterization of the osteocyte lacunar system. *Bone* **57**, 142–154 (2013).

93. Obata, Y. *et al.* Quantitative and qualitative bone imaging: A review of synchrotron radiation microtomography analysis in bone research. *J. Mech. Behav. Biomed. Mater.* **110**, 103887 (2020).

94. Portier, H., Jaffré, C., Kewish, C. M., Chappard, C. & Pallu, S. New insights in osteocyte imaging by synchrotron radiation. *J. Spectr. Imaging* **9**, 1–29 (2020).

95. Akhter, M. P. & Recker, R. R. High resolution imaging in bone tissue research-review. *Bone* 115620 (2020).

96. Pfeiffer, F. X-ray ptychography. *Nat. Photonics* **12**, 9–17 (2018).

97. Bazin, D. *et al.* Diffraction techniques and vibrational spectroscopy opportunities to characterise bones. *Osteoporos. Int.* **20**, 1065–1075 (2009).

98. Morris, M. D. & Mandair, G. S. Raman assessment of bone quality. *Clin. Orthop. Relat. Res.* **469**, 2160–2169 (2011).

99. Mandair, G. S. & Morris, M. D. Contributions of Raman spectroscopy to the understanding of bone strength. *Bonekey Rep.* **4**, 1–8 (2015).

100. Paschalis, E. P., Gamsjaeger, S. & Klaushofer, K. Vibrational spectroscopic techniques to assess bone quality. *Osteoporos. Int.* 1–17 (2017).

101. Gamsjaeger, S. *et al.* Cortical bone composition and orientation as a function of animal and tissue age in mice by Raman spectroscopy. *Bone* **47**, 392–399 (2010).

102. Roschger, A. *et al.* Relationship between the v_2PO_4/amide III ratio assessed by Raman spectroscopy and the calcium content measured by quantitative backscattered electron microscopy in healthy human osteonal bone. *J. Biomed. Opt.* **19**, 065002 (2014).

103. Yerramshetty, J. S., Lind, C. & Akkus, O. The compositional and physicochemical homogeneity of male femoral cortex increases after the sixth decade. *Bone* **39**, 1236–43 (2006).

104. Juang, C., Finzi, L. & Bustamante, C. J. Design and application of a computer-controlled confocal scanning differential polarization microscope. *Rev. Sci. Instrum.* **59**, 2399–2408 (1988).

105. Taylor, N. W. & Sheard, C. Microscopic and x-ray investigations on the calcification of tissue. *J. Biol. Chem.* **81**, 479–493 (1928).

106. Ascenzi, A. & Fabry, C. Technique for Dissection and Measurement of Refractive Index. *J. Biophys. Biochem. Cytol.* **6**, 139–143 (1959).

107. Aparicio, S. *et al.* Optimal methods for processing mineralized tissues for Fourier transform infrared microspectroscopy. *Calcif. Tissue Int.* **70**, 422–429 (2002).

108. Boskey, A. & Pleshko Camacho, N. FT-IR imaging of native and tissue-engineered bone and cartilage. *Biomaterials* **28**, 2465–2478 (2007).

109. Boskey, A. & Mendelsohn, R. Infrared analysis of bone in health and disease. *J. Biomed. Opt.* **10**, 031102 (2005).

110. Goldstein, J. I. *et al. Scanning electron microscopy and X-ray microanalysis*. (Springer, 2017).

111. Arnal, F., Verdier, P. & Vincensini, P. Coefficient of backscattering in the case of monoelectric electrons arriving at the target with an oblique incidence. *Compt rend Acad Sci* **B 268**, 1526–1529 (1969).

112. Howell, P. G. T., Davy, K. M. W. & Boyde, A. Mean atomic number and backscattered electron coefficient calculations for some materials with low mean atomic number. *Scanning* **20**, 35–40 (1998).

113. Campbell, S. E., Geiss, R. H., Feller, S. A. & Ferguson, V. L. Tunable glass reference materials for quantitative backscattered electron imaging of mineralized tissues. *J. Mater. Res.* **27**, 2568–2577 (2012).

114. Skedros, J. G., Bloebaum, R. D., Bachus, K. N., Boyce, T. M. & Constantz, B. Influence of mineral content and composition on graylevels in backscattered electron images of bone. *J. Biomed. Mater. Res.* (1993).

115. Roschger, P., Fratzl, P., Eschberger, J. & Klaushofer, K. Validation of quantitative backscattered electron imaging for the measurement of mineral density distribution in human bone biopsies. *Bone* **23**, 319–326 (1998).

116. Heveran, C. M. *et al.* Moderate chronic kidney disease impairs bone quality in C57Bl/6J mice. *Bone* **86**, 1–9 (2016).

117. Roschger, P. *et al.* Alendronate increases degree and uniformity of mineralization in cancellous bone and decreases the porosity in cortical bone of osteoporotic women. *Bone* **29**, 185–191 (2001).

118. Tamminen, I. S. *et al.* Increased heterogeneity of bone matrix mineralization in pediatric patients prone to fractures: A biopsy study. *J. Bone Miner. Res.* **29**, 1110–1117 (2014).

119. Ferguson, V. L., Bushby, A. J. & Boyde, A. Nanonmechanical properties and mineral concentration in articular calcified cartilage and subchondral bone. *J. Anat.* **203**, 191–202 (2003).

120. Boyde, A., Travers, R., Glorieux, F. H. & Jones, S. J. The mineralization density of iliac crest bone from children with osteogenesis imperfecta. *Calcif. Tissue Int.* **64**, 185–190 (1999).

121. Müllerová, I. & Frank, L. Contrast at Very Low Energies of the Gold/Carbon Specimen for Resolution Testing. *Scanning* **26**, 18–24 (2004).

122. Lewis, P. *et al.* Exploring backscattered imaging in low voltage FE-SEM. *J. Phys. Conf. Ser.* **644**, (2015).

123. Howell, P. G. T. & Boyde, A. Monte Carlo simulations of electron scattering in bone. *Bone* **15**, 285–291 (1994).

124. Newbury, D. E. & Ritchie, N. W. M. Performing elemental microanalysis with high accuracy and high precision by scanning electron microscopy/silicon drift detector energy-dispersive X-ray spectrometry (SEM/SDD-EDS). *J. Mater. Sci.* **50**, 493–518 (2014).

125. Newbury, D. E. & Ritchie, N. W. M. Electron-excited X-ray microanalysis at low beam energy: Almost always an adventure! *Microsc. Microanal.* **22**, 735–753 (2016).

126. Kourkoumelis, N., Balatsoukas, I. & Tzaphlidou, M. Ca/P concentration ratio at different sites of

normal and osteoporotic rabbit bones evaluated by Auger and energy dispersive X-ray spectroscopy. *J. Biol. Phys.* **38**, 279–291 (2012).

127. Ritchie, N. W. M. M icroscopy M icroanalysis Spectrum Simulation in DTSA-II. 454–468 (2009).

128. Gunawardane, R. P. & Arumainayagam, C. R. AUGER ELECTRON SPECTROSCOPY\nHandbook of Applied Solid State Spectroscopy. *Handb. Appl. Solid State Spectrosc.* 451–483 (2006).

129. Ong, J. L. & Lucas, L. C. Auger electron spectroscopy and its use for the characterization of titanium and hydroxyapatite surfaces. *Biomaterials* **19**, 455–464 (1998).

130. Miller, R. G., Bowles, C. Q., Gutshall, P. L. & Eick, J. D. The Effects of Ion Sputtering on Dentin and its Relation to Depth Profiling. *J. Dent. Res.* **73**, 1457–1461 (1994).

131. Tzaphlidou, M., Berillis, P. & Matthopoulos, D. Bone calcium, phosphorus detection by Auger electron spectroscopy. *Micron* **36**, 706–709 (2005).

132. Sundgren, J. E., Bodö, P. & Lundström, I. Auger electron spectroscopic studies of the interface between human tissue and implants of titanium and stainless steel. *J. Colloid Interface Sci.* **110**, 9–20 (1986).

133. Miller, R. G., Bowles, C. Q., Eick, J. D. & Gutshall, P. L. Auger electron spectroscopy of dentin: elemental quantification and the effects of electron and ion bombardment. *Dent. Mater.* **9**, 280–285 (1993).

134. Everts, V., Niehof, A., Tigchelaar-Gutter, W. & Beersten, W. Transmission Electron Microscopy of Bone. in *Methods in Molecular Biology* **816**, 351–363 (2012).

135. Schwarcz, H. P., McNally, E. A. & Botton, G. A. Dark-field transmission electron microscopy of cortical bone reveals details of extrafibrillar crystals. *J. Struct. Biol.* **188**, 240–248 (2014).

136. Rubin, M. A. *et al.* TEM analysis of the nanostructure of normal and osteoporotic human trabecular bone. *Bone* **33**, 270–282 (2003).

137. Suvorova, E. I., Petrenko, P. P. & Buffat, P. A. Scanning and transmission electron microscopy for evaluation of order/disorder in bone structure. *Scanning* **29**, 162–170 (2007).

138. Suvorova, E. I., Buffat, P. A., Layrolle, P., Bouler, J. M. & Dacolsi, G. Electron diffraction and high resolution transmission electron microscopy in the characterization of calcium phosphate precipitation from aqueous solutions under biomineralization conditions. *Eur. Cells Mater.* **1**, 27–42 (2001).

139. Akhter, M. P., Kimmel, D. B., Lappe, J. M. & Recker, R. R. Effect of macroanatomic bone type and estrogen loss on osteocyte lacunar properties in healthy adult women. *Calcif. Tissue Int.* **100**, 619–630 (2017).

140. Hemmatian, H., Laurent, M. R., Claessens, F., Vanderschueren, D. & Lenthe, G. H. van. 3D assessment of mouse cortical bone microstructural architecture by desktop micro-CT. (2016).

141. Lau, S. H. *et al.* Multiscale 3D Bioimaging: from cell, tissue to whole organism. in *Scanning Microscopy 2009* **7378**, 73781V (International Society for Optics and Photonics, 2009).

142. Langer, M. *et al.* X-Ray Phase Nanotomography Resolves the 3D Human Bone Ultrastructure. *PLoS One* **7**, 1–7 (2012).

143. Peyrin, F., Dong, P., Pacureanu, A. & Langer, M. Micro- and Nano-CT for the Study of Bone

Ultrastructure. *Curr. Osteoporos. Rep.* **12**, 465–474 (2014).

144. Larrue, A., Rattner, A., Laroche, N., Vico, L. & Peyrin, F. Feasibility of micro-crack detection in human trabecular bone images from 3D synchrotron microtomography. *Annu. Int. Conf. IEEE Eng. Med. Biol. - Proc.* 3918–3921 (2007).

145. Brock, G. R. *et al.* Nanoscale Examination of Microdamage in Sheep Cortical Bone Using Synchrotron Radiation Transmission X-Ray Microscopy. *PLoS One* **8**, 4–12 (2013).

146. Larrue, A. *et al.* Synchrotron radiation micro-CT at the Micrometer scale for the analysis of the three-dimensional morphology of microcracks in human trabecular bone. *PLoS One* **6**, (2011).

147. Mürer, F. K. *et al.* 3D Maps of Mineral Composition and Hydroxyapatite Orientation in Fossil Bone Samples Obtained by X-ray Diffraction Computed Tomography. *Sci. Rep.* **8**, 10052 (2018).

148. Seidel, R. *et al.* Synchrotron 3D SAXS analysis of bone nanostructure. *Bioinspired, Biomim. Nanobiomaterials* **1**, 123–132 (2012).

149. Wagermaier, W. *et al.* Scanning texture analysis of lamellar bone using microbeam synchrotron radiation. *Acta Crystallogr. Sect. A Found. Crystallogr.* **61**, c311–c311 (2005).

150. Wagermaier, W. *et al.* Spiral twisting of fiber orientation inside bone lamellae. *Biointerphases* **1**, 1–5 (2006).

151. Dierolf, M. *et al.* Ptychographic X-ray computed tomography at the nanoscale. *Nature* **467**, 436–439 (2010).

152. Hawkes, P. W. & Spence, J. C. H. *Handbook Microscopy*. (2019).

153. Holler, M. *et al.* X-ray ptychographic computed tomography at 16 nm isotropic 3D resolution. *Sci. Rep.* **4**, 1–5 (2014).

154. Ciani, A. *et al.* Ptychographic X-ray CT characterization of the osteocyte lacuno-canalicular network in a male rat's glucocorticoid induced osteoporosis model. *Bone reports* **9**, 122–131 (2018).

155. Oyen, M. L. & Cook, R. F. A practical guide for analysis of nanoindentation data. *J. Mech. Behav. Biomed. Mater.* **2**, 396–407 (2009).

156. Campbell, S. E., Ferguson, V. L. & Hurley, D. C. Nanomechanical mapping of the osteochondral interface with contact resonance force microscopy and nanoindentation q. *Acta Biomater.* **8**, 4389–4396 (2012).

157. Hurley, D. C. Contact Resonance Force Microscopy Techniques for Nanomechanical Measurements. *Appl. Scanning Probe Methods* **XI**, 97–138 (2009).

158. Fischer-Cripps, A. C. *Nanoindentation*. (Springer, 2004).

159. Ebenstein, D. M. & Pruitt, L. A. Nanoindentation of biological tissues. *Nano Today* **1**, 26–33 (2006).

160. Labonte, D., Lenz, A.-K. & Oyen, M. L. On the relationship between indenation hardness and modulus, and the damage resistance of biological materials. *Acta Biomater.* **57**, 373–383 (2017).

161. Rodriguez-Florez, N., Oyen, M. L. & Shefelbine, S. J. Insight into differences in nanoindentation properties of bone. *J. Mech. Behav. Biomed. Mater.* **18**, 90–99 (2013).

162. Pathak, S. *et al.* Measuring the dynamic mechanical response of hydrated mouse bone by

nanoindentation. *J. Mech. Behav. Biomed. Mater.* **4**, 34–43 (2011).

163. Kopycinska-Müller, M., Geiss, R. H. & Hurley, D. C. Contact mechanics and tip shape in AFM-based nanomechanical measurements. *Ultramicroscopy* **106**, 466–474 (2006).

164. Carden, A. & Morris, M. D. Application of vibrational spectroscopy to the study of mineralized tissues (review). *J. Biomed. Opt.* **5**, 259 (2000).

165. Knapp, H. F., Reilly, G. C., Stemmer, A., Niederer, P. & Knothe Tate, M. L. Development of preparation methods for and insights obtained from atomic force microscopy of fluid spaces in cortical bone. *Scanning* **24**, 25–33 (2002).

166. Feng, J. Q. *et al.* Loss of DMP1 causes rickets and osteomalacia and identifies a role for osteocytes in mineral metabolism. *Nat Genet* **38**, 1310–1315 (2006).

167. Mabilleau, G., Perrot, R., Flatt, P. R., Irwin, N. & Chappard, D. High fat-fed diabetic mice present with profound alterations of the osteocyte network. *Bone* **90**, 99–106 (2016).

168. Newbury, D. E. & Ritchie, N. W. Is Scanning Electron Microscopy / Energy Dispersive X-ray Spectrometry (SEM / EDS) Quantitative ? *Scanning* **35**, 141–168 (2013).

169. Lai, X. *et al.* The dependences of osteocyte network on bone compartment, age, and disease. *Bone Res.* **3**, 15009 (2015).

170. Stampanoni, M. *et al.* Trends in synchrotron-based tomographic imaging: the SLS experience. in *Proc.SPIE* **6318**, (2006).

171. Chappard, C. *et al.* 3D characterization of pores in the cortical bone of human femur in the elderly at different locations as determined by synchrotron micro-computed tomography images. *Osteoporos. Int.* **24**, 1023–1033 (2013).

172. Schneider, P. *et al.* Ultrastructural properties in cortical bone vary greatly in two inbred strains of mice as assessed by synchrotron light based micro-and nano-CT. *J. Bone Miner. Res.* **22**, 1557–1570 (2007).

173. Yu, B., Pacureanu, A., Olivier, C., Cloetens, P. & Peyrin, F. Assessment of the human bone lacuno-canalicular network at the nanoscale and impact of spatial resolution. *Sci. Rep.* **10**, 1–12 (2020).

174. Djomehri, S. I. *et al.* Mineral density volume gradients in normal and diseased human tissues. *PLoS One* **10**, e0121611 (2015).

175. Kazakia, G. J., Burghardt, A. J., Cheung, S. & Majumdar, S. Assessment of bone tissue mineralization by conventional x-ray microcomputed tomography: Comparison with synchrotron radiation microcomputed tomography and ash measurements. *Med. Phys.* **35**, 3170–3179 (2008).

176. Nuzzo, S. *et al.* Synchrotron Radiation Microtomography Allows the Analysis of Three-Dimensional Microarchitecture and Degree of Mineralization of Human Iliac Crest Biopsy Specimens: Effects of Etidronate Treatment. *J. Bone Miner. Res.* **17**, 1372–1382 (2002).

177. Weitkamp, T. *et al.* Parallel-beam imaging at the ESRF beamline ID19: current status and plans for the future. *AIP Conf. Proc.* **1234**, 83–86 (2010).

178. Shahmoradian, S. H. *et al.* Three-dimensional imaging of biological tissue by cryo x-ray ptychography. *Sci. Rep.* **7**, 1–12 (2017).

179. Langer, M. & Peyrin, F. 3D X-ray ultra-microscopy of bone tissue. *Osteoporos. Int.* **27**, 441–455

(2016).

180. Lin, Y. & Xu, S. AFM analysis of the lacunar-canalicular network in demineralized compact bone. *J. Microsc.* **241**, 291–302 (2011).

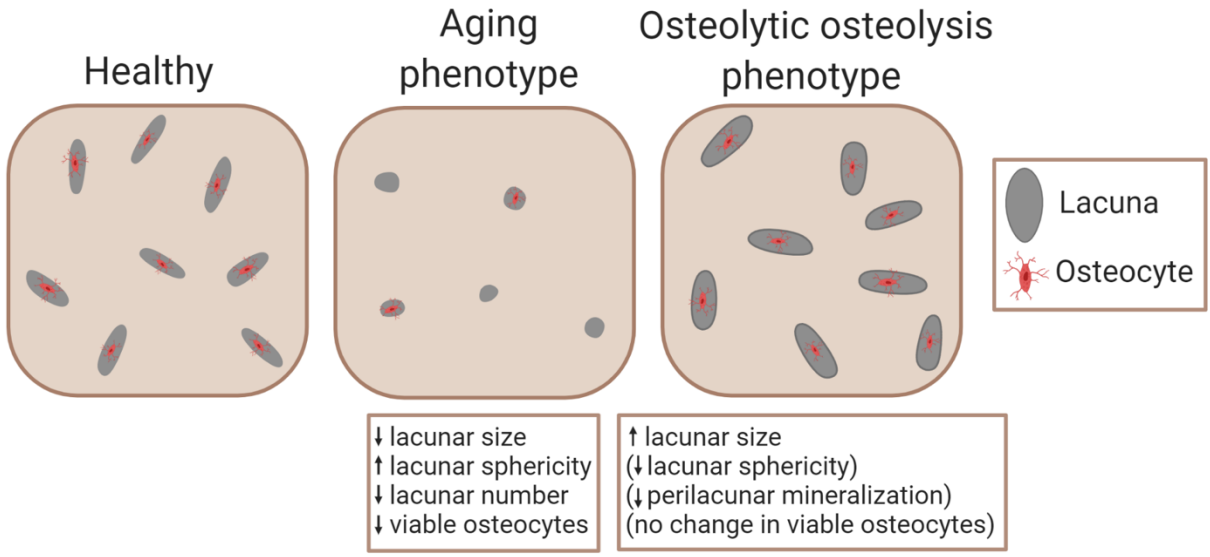

Figure 1. Two phenotypes for LCS remodeling. Compared with healthy reference bone, the 'aging' phenotype is associated with smaller, more spherical, and fewer lacunae, with higher osteocyte apoptosis. The 'osteolytic osteolysis' phenotype is more variable. In all cases, lacunae and canaliculi are enlarged. Sometimes lacunae are elongated and surrounded by less-mineralized bone, while osteocyte viability usually does not decrease.

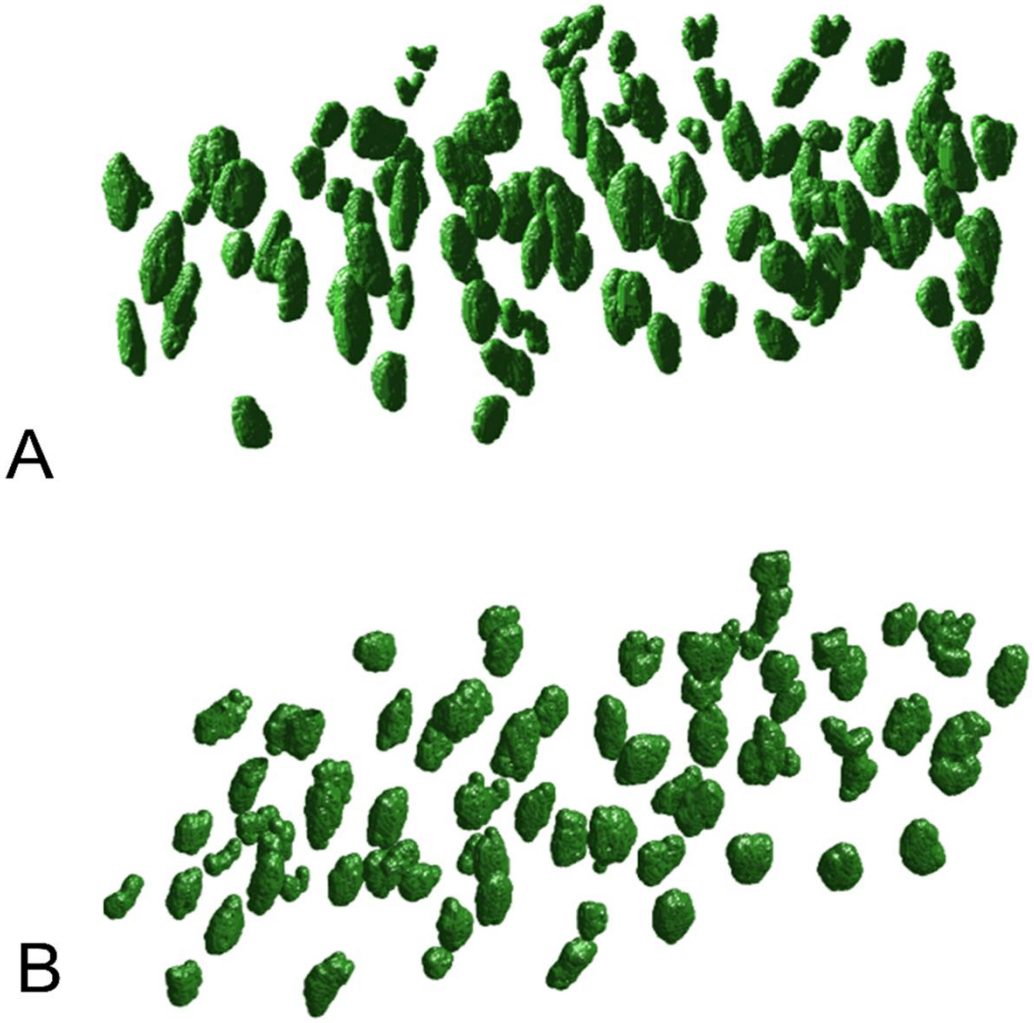

Figure 2. 3D osteocyte lacunar geometries change with age. Compared with 6-month male mice (A), lacunae in bones from 24-month male mice (B) are smaller, more spherical, and sparser. (reprinted from[15])

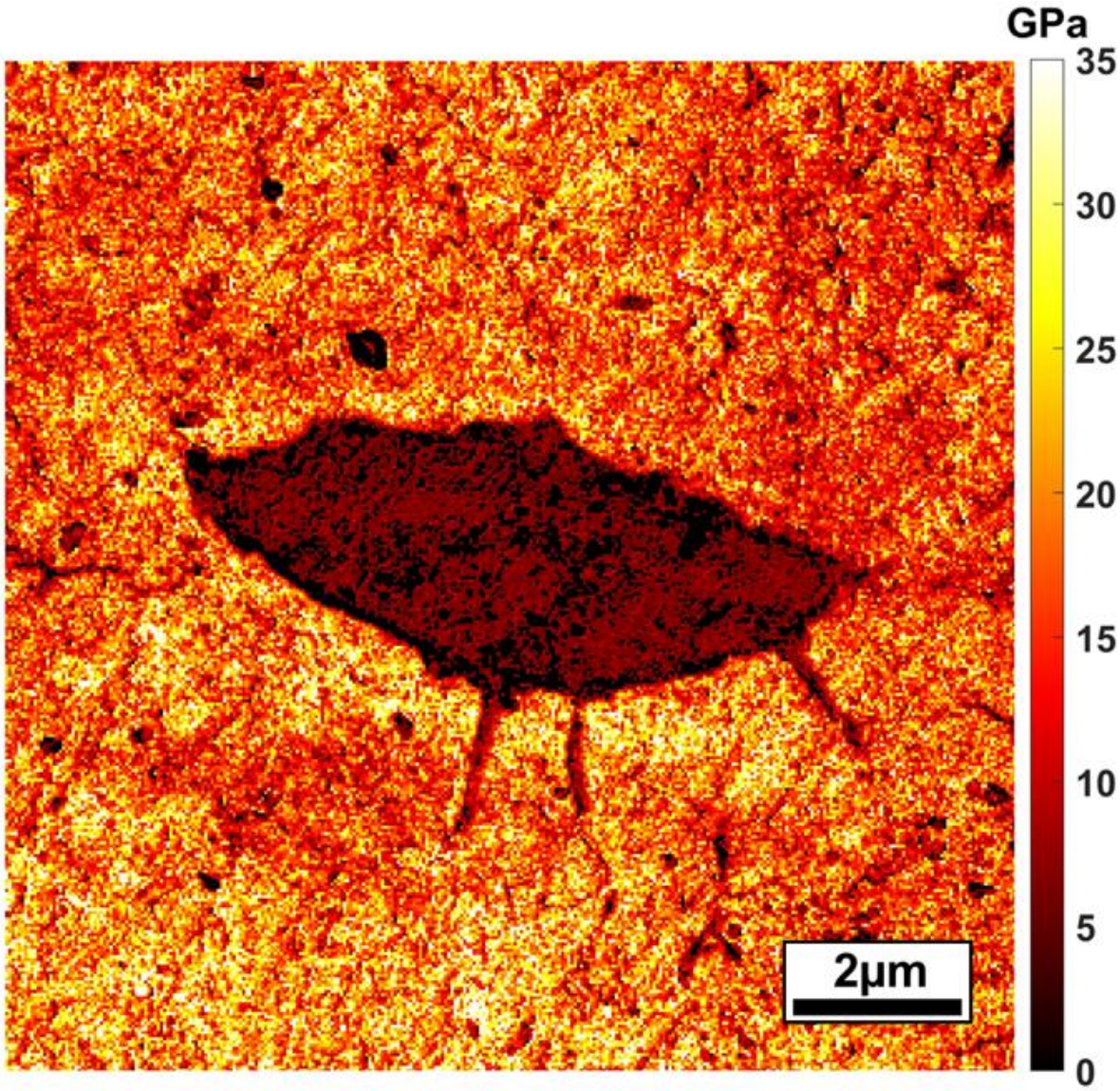

Figure 3. Bone tissue modulus varies at the submicroscale surrounding an osteocyte lacuna. This modulus map was generated for PMMA-embedded and polished murine bone using atomic force microscopy.